Electrochimica Acta 53 (2008) 8103–8117

Contents lists available at ScienceDirect

Electrochimica Acta

journal homepage: www.elsevier.com/locate/electacta

Review

Recent progress in electrodeposition of thermoelectric thin films and nanostructures

Feng Xiao [a], Carlos Hangarter [a], Bongyoung Yoo [b], Youngwoo Rheem [a], Kyu-Hwan Lee [c], Nosang V. Myung [a,*]

[a] Department of Chemical and Environmental Engineering, University of California-Riverside, Riverside, CA 92521, United States
[b] Division of Materials and Chemical Engineering, Hanyang University, Ansan 426-791, South Korea
[c] Electrochemical Processing Group, Korea Institute of Materials Science, Changwon-Si, Kyungnam 641-010, South Korea

ARTICLE INFO

Article history:
Received 17 January 2008
Received in revised form 6 June 2008
Accepted 7 June 2008
Available online 20 June 2008

Keywords:
Thermoelectric
Nanowires
Superlattice thin films
Thin films
Electrodeposition
Seebeck
Peltier

ABSTRACT

Thermoelectric power generators and coolers have many advantages over conventional refrigerators and power generators such as solid-state operation, compact design, vast scalability, zero-emissions and long operating lifetime with no maintenance. However, the applications of thermoelectric devices are limited to where their unique advantages outweigh their low efficiency. Despite this practical confine, there has been a reinvigorated interest in the field of thermoelectrics through identification of classical and quantum mechanical size effects, which provide additional ways to enhance energy conversion efficiencies in nanostructured materials. Although, there are a few reports which demonstrated the improvement of efficiency through nanoengineering, the successful application of these nanostructures will be determined by a cost-effective and high through-put fabrication method. Electrodeposition is the method of choice to synthesize nanoengineered thermoelectric materials because of low operating and capital cost, high deposition rates, near room temperature operation, and the ability to tailor the properties of materials by adjusting deposition conditions. In this paper, we reviewed the recent progress of the electrodeposition of thermoelectric thin films and nanostructures including Bi, $Bi_{1-x}Sb_x$, Bi_2Te_3, Sb_2Te_3, $(Bi_{1-x}Sb_x)_2Te_3$, Bi_2Se_3, $Bi_2Te_{3-y}Se_y$, PbTe, PbSe, $PbSe_{1-x}Te_x$ and $CoSb_3$.

Contents

1. Introduction 8104
2. Electrodeposition of thermoelectric thin films and nanowires 8104
   2.1. Electrodeposition of bismuth 8104
   2.2. Electrodeposition of $Bi_{1-x}Sb_x$ 8106
   2.3. Electrodeposition of Bi_2Te_3 8107
   2.4. Electrodeposition of Sb_2Te_3 and $(Bi_{1-x}Sb_x)_2Te_3$ 8110
   2.5. Electrodeposition of Bi_2Se_3 and $Bi_2Te_{3-y}Se_y$ 8112
   2.6. Electrodeposition of PbTe 8112
   2.7. Electrodeposition of PbSe and $PbSe_{1-x}Te_x$ 8113
   2.8. Electrodeposition of $CoSb_3$ 8114
3. Device fabrication 8115
4. Conclusion 8116
   Acknowledgements 8116
   References 8116

* Corresponding author at: Bourns Hall B353, Department of Chemical and Environmental Engineering, University of California-Riverside, Riverside, CA 92521, United States. Tel.: +1 951 827 7710; fax: +1 951 827 5696.
E-mail address: myung@engr.ucr.edu (N.V. Myung).

0013-4686/$ – see front matter © 2008 Elsevier Ltd. All rights reserved.
doi:10.1016/j.electacta.2008.06.015

1. Introduction

The growing concern over increasing energy cost and global warming associated with fossil fuel sources has stimulated the search for cleaner, more sustainable energy sources. Among the viable technologies, thermoelectric (TE) energy converters have received attention as these solid-state devices can generate electricity by harvesting waste thermal energy, thereby improving the efficiency of a system. The many advantages of TE devices include solid-state operation, zero-emissions, vast scalability, no maintenance and a long operating lifetime. The efficiency of TE materials is directly related to a dimensionless figure of merit ZT which is defined as:

$$\mathrm{ZT} = \frac{S^2\sigma}{\kappa}T \quad (1)$$

where S is the Seebeck coefficient, σ the electrical conductivity, κ the thermal conductivity and T is the absolute temperature.

In order to compete with conventional refrigerators, a ZT of 3 is required. Due to their limited energy conversion efficiencies (i.e. ZT is ~1), thermoelectric devices currently have a rather narrow set of applications. However, there is a reinvigorated interest in the field of thermoelectrics due to classical and quantum mechanical size effects, which provide additional ways to enhance energy conversion efficiencies in nanostructured materials [1–5]. For example, a ZT up to 2.5 was achieved by synthesizing two-dimensional Sb_2Te_3/Bi_2Te_3 superlattice thin films through a chemical vapor deposition (CVD) process, exceeding previous limits of ~1 for bulk counterparts [6]; theoretical calculations predict that even higher ZTs can be achieved in one-dimensional nanowires (Fig. 1) [7].

The successful application of these nanostructures in practical thermoelectric devices must implement a cost-effective and high through-put fabrication process. Various techniques have been applied to synthesize nanostructured thermoelectric materials such as chemical vapor deposition (CVD) [6], molecular beam epitaxy (MBE) [8], vapor–liquid–solid growth process [9], hydrothermal process [10], and electrodeposition. Compared to other methods, electrodeposition is one the most cost-effective techniques for the fabrication of nanostructured materials. The advantage of electrodeposition includes: room temperature operation, thus reducing problems with thermal stress; low equipment cost, no vacuum required; high deposition rates; and easy scalability. Furthermore, miniaturization of thermoelectric devices have thus far been fabricated more successfully by an electrodeposition process than other deposition techniques [11]. A variety of TE materials, i.e. Bi, $Bi_{1-x}Sb$, Bi_2Te_3, Sb_2Te_3, $(Bi_{1-x}Sb_x)_2Te_3$, Bi_2Se_3, $Bi_2Te_{3-y}Se_y$, PbTe, PbSe, $PbSe_{1-x}Te_x$ and $CoSb_3$, have been synthesized by electrodeposition technique. In this paper, we review the recent progress on the electrodeposition of thermoelectric thin films and nanowires.

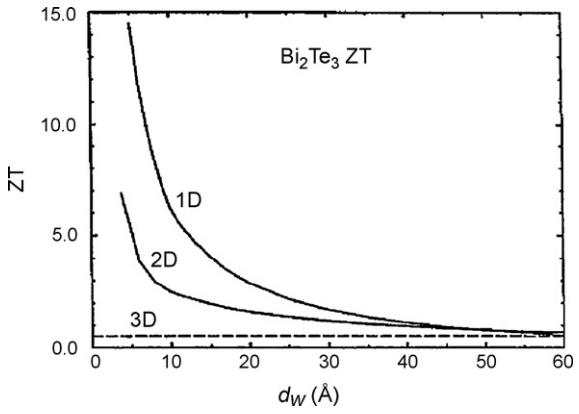

Fig. 1. Calculated dependence of ZT within the quantum well or quantum wire on the well or wire width for a Bi_2Te_3-like material at the optimum doping level for transport in the highest mobility direction. Also shown is the ZT for bulk Bi_2Te_3 calculated using the corresponding 3D model. Reprinted with permission from ref. [7]. Copyright [1999] Taylor and Francis.

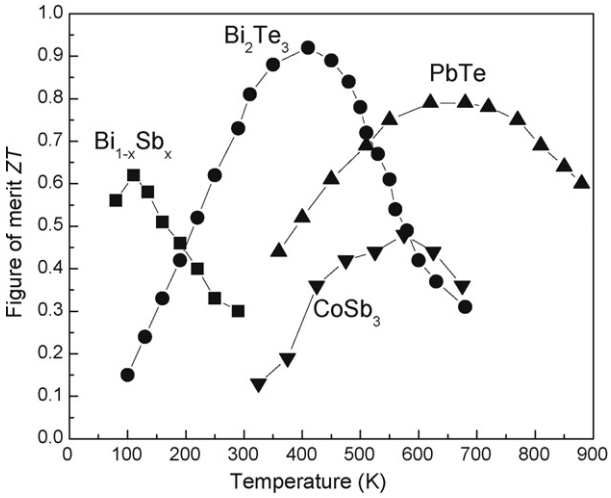

Fig. 2. The thermoelectric figure-of-merit (ZT) as a function of operating temperature. Reprinted with permission from ref. [17]. Copyright [1999] American Association for the Advancement of Science.

2. Electrodeposition of thermoelectric thin films and nanowires

Table 1 lists the thermoelectric materials which have been synthesized by electrodeposition and their bulk properties at optimum doping level [12–16]. No single material is suited for all temperature ranges as the ZT values strongly depend on the operating temperature (Fig. 2) [12,17]. $Bi_{1-x}Sb_x$ performs best near liquid nitrogen temperatures and is used for low temperature application. Bi_2Te_3 based alloys show the highest performance near room temperature and are mainly used for cooling applications. PbTe and $CoSb_3$ based alloys work better around 600 K, being primarily employed for power generation. The following sections review the recent progress of electrodeposited thermoelectric materials.

2.1. Electrodeposition of bismuth

Bi has a rhombohedral structure with a low melting point of 271.4 °C, which is slightly distorted from a cubic structure [18]. For bulk Bi, the ZT is very low (ZT of ~0) because of the overlap between conduction and valence bands (~38 meV), which means that the contributions of holes and electrons to S cancel each other. However, a semimetal-to-semiconductor transition has been predicted for Bi nanowires below a critical size (~50 nm depending on the crystal orientation) due to quantum-confinement effects (Fig. 3) [19–21]. Therefore, S is predicted to be significantly enhanced for Bi nanowires with an optimized position of the Fermi energy, sharply peaked density of electron states [22,23]. Bi nanowires also have a reduced thermal conductivity due to phonon scattering at the side walls which helps to increase ZT [20,21]. For 5 nm Bi nanowires oriented along the trigonal axis at 77 K, the maximum ZT of 6 with an optimized carrier concentration 10^{18} cm was predicted. The ZT value is also strongly dependent on the wire orientation due to the anisotropic nature of Bi [20]. Unfortunately, most work to date on Bi does not report on its thermoelectric properties, as most

Table 1
The thermoelectric properties of bulk materials

Materials	Optimum composition	Highest Z (10^{-3} K^{-1})	Seebeck coefficient (μV K^{-1})	Electrical resistivity ($\mu\Omega$ m)	Thermal conductivity (Wm^{-1} K^{-1})	Band-gap energy (meV)
$Bi_{1-x}Sb_x$	x = 0.16–0.18, n-type	7 (60 K)	−160	1.5	2.4	20
Bi_2Te_3	64.5 at.% Te, n-type	2.89 (300 K)	−240	10	2.02	160
	54.3 at.% Te, p-type	2.32 (300 K)	162	5.5	2.06	
Sb_2Te_3	72.5 at.% Te, p-type	1.61 (300 K)	92	3.23	1.63	250–300
$(Bi_{1-x}Sb_x)_2Te_3$	x = 0.75–0.8, p-type	3.2 (300 K)	206	8.89	1.49	190
$Bi_2Te_{3-y}Se_y$	y = 0.075–0.15, p-type	2.89 (300 K)	230	11.05	1.66	175
PbTe	Unknown, n-type	1.6 (673 K)				320
	Unknown, p-type	1.2 (673 K)				
$CoSb_3$	Unknown, p-type	1.47 (573 K)	220	10.3	3.2	320

groups have instead focused on its metal-to-semiconductor transition of electrical properties and magnetoresistance (MR) properties instead.

The magnetoresistance in Bi is a product of its large anisotropy and unique semimetal properties, which Chien et al. have rigorously investigated. In their early work, they electrodeposited Bi thin films [24–27] from acidic aqueous solutions containing 0.15 M $Bi(NO_3)_3$ + 1 M KNO_3 + 0.33 M 2*R*,3*R*-$(CHOHCOOH)_2$ (L-tartaric acid) + 0.65 M HNO_3 with 10 vol.% glycerol (pH 0.1–0.2). This electrolyte was relatively concentrated and highly complexed with deposition carried out at −30 mV versus the Ag/AgCl (3 M NaCl) reference electrode, with Pt serving as the counter electrode. They initially used gold (10 nm thick) sputtered onto Si(1 0 0) wafers as the working electrodes for Bi film deposition. Polycrystalline 1–20 μm thick Bi films were deposited at a rate of ∼0.2 μm/min at room temperature. The as-deposited films were polycrystalline with large grains (up to a few micrometers), but after annealing in an inert environment (i.e. argon) at 268 °C for 6 h, they became single crystals with the trigonal axis [1 1 1] perpendicular to the film plane [24]. When Bi was electrodeposited on p-GaAs (1 0 0), the as-deposited Bi films were polycrystalline with no preferred orientation and the grain size was close to the film thickness. After annealing, the grain size became much larger than the film thickness, but the films were still polycrystalline with a preferential (0 1 2) orientation instead of the single crystal [1 1 1] orientation on gold substrates [25].

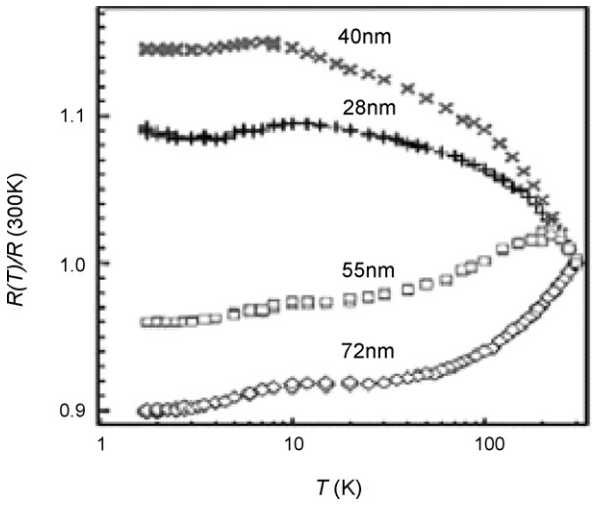

Fig. 3. The temperature dependent resistance of Bi nanowire with the diameter equal to 72, 55, 40, and 28 nm, respectively. The resistance was normalized to the resistance at 300 K. Each point in the plot was obtained by fitting a four-point *I*–*V* trace [19]. Reprinted with permission from ref. [19]. Copyright [2006] Wiley-VCH Verlag GmbH & Co. KGaA.

Chien's group [28] also investigated the electrodeposition of Bi films on an alternate substrate, p-GaAs (1 1 0) wafers, from a solution containing 0.02 M BiO^+ (from Bi_2O_3) in 2 M $HClO_4$. They first applied a short (0.1–0.25 s) nucleation pulse at −0.275 V vs. Ag/AgCl (3 M NaCl) and followed with a low deposition potential of −0.02 or −0.025 V. During the initial nucleation pulse, the current density was varied from 5 to 40 mA/cm^2, corresponding to 1–5 nm of bismuth. The as-deposited films up to 1 μm thick were polycrystalline with a preferential (0 1 8) orientation.

Despite the high crystallinity and MR values for films electrodeposited by Chien's group, Sadale and Patil [29] were one of the first to conduct a systematic study on the nucleation and growth of bismuth thin films. They utilized cyclic voltammetry and chronoamperometry with fluorine doped tin oxide (FTO) substrate and a nitrate bath. The solutions of different Bi^{3+} concentrations (0.0001–50 mM) were prepared by dissolving $Bi(NO_3)_3{\cdot}5H_2O$ in double-distilled water. Triethanolamine (TEA) was used to complex the Bi ions. When the applied potential was between −250 and −300 mV vs. SCE, the nucleation of Bi took place via a three-dimensional progressive nucleation and growth under diffusive and partial kinetic control. For a potential between −350 and −500 mV, Bi nucleated via a three-dimensional instantaneous nucleation and growth under diffusive control. Bi electrodeposition at lower concentrations (<1 mM) did not follow simple instantaneous or progressive nucleation models. The Bi thin films deposited from higher Bi^{3+} concentrations were preferably oriented along {1 0 4} planes, whereas those deposited from lower Bi^{3+} concentrations (<0.1 mM) were either amorphous or microcrystalline. Yang and Hu [30] investigated the nucleation and growth of bismuth thin films on glassy carbon electrodes utilizing the same techniques as Sadale and Patil.

Chien and co-workers [31–33] were also among the first to synthesize and electrically characterize electrodeposited Bi nanowires arrays utilizing a template-directed electrodeposition with polycarbonate membranes as scaffolds. The plating solutions were similar to their prior works. A thin layer of Au was first sputtered on one side of the membrane serving as the working electrode. X-ray diffraction of the Bi nanowires revealed a rhombohedral structure with no preferred orientation. According to the dark field image by TEM, the Bi nanowire had an oxide shell layer and the crystal grains were typically two to four times that of the wire diameter. The oxide layer did not come into play when characterizing the nanowires since the measurements were conducted in an array fashion within the template.

Jin et al. [34] later synthesized Bi nanowires by potentiostatic electrodeposition using anodized alumina with pore diameter of 60 nm. The electrolytes employed were acidic nitrate baths with

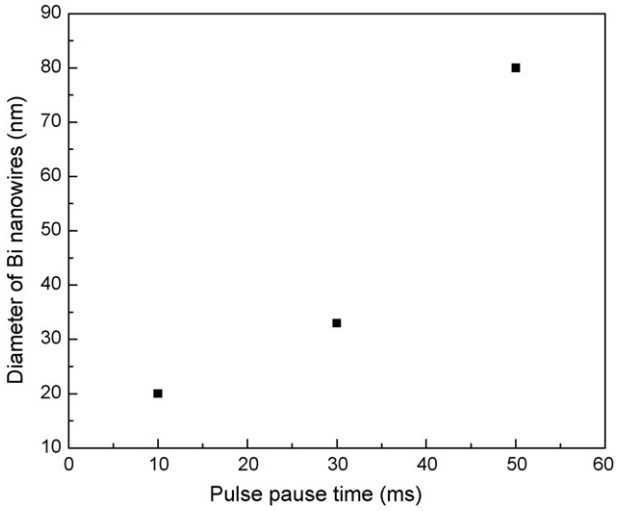

Fig. 4. The diameter of Bi nanowires vs. the pulse pause time when the pulse on time was fixed at 10 ms [37].

glycerol. Li et al. [35–38] also reported the pulsed electrodeposition of single crystalline Bi nanowires in anodic alumina. The electrolytes contained 0.13 M $BiCl_3$ + 0.33 M tartaric acid + 1.3 M glycerol + 1.2 M NaCl + 1 M HCl. The pH was adjusted to ~1 by adding 5 M NH_4OH. The pulse plating was carried out under modulated potential control between a graphite anode and nanotemplate cathode in a two-electrode cell. The as-deposited Bi nanowires were single crystal. The crystal orientation of the Bi nanowires was very sensitive to the applied potential, pulse duration (t_{on}) and pulse pause time (t_{off}). When the applied potential was fixed at −0.35 V and the pulse duration was 10 ms, the Bi nanowires were oriented along (0 2 2) direction [37]. With a deposition potential of −0.9 V and pulse duration ≤30 ms, the nanowires were oriented along (1 1 0) direction; but with a pulse duration >30 ms, the nanowire orientation changed to (2 0 2) direction [35,36]. The diameter of Bi nanowires was also adjusted by controlling the pulse duration time or pulse pause time. Fig. 4 shows the diameter of Bi nanowires deposited at −0.35 V vs. the pulse pause time [37].

More recently, they demonstrated the fabrication of Bi nanotubes using template-directed pulse electrodeposition [39]. The fabrication process for nanotubes is similar to Bi nanowires except that the thickness of sputtered gold seed layers was reduced to build up around the wall of each pore instead of forming a continuous film (Fig. 5b). Then, the subsequent electrodeposition of Bi took place only on Au covered areas resulting in the growth of Bi along the pore walls, and thus forming the tubular nanostructure. Restricting the proceeding electrodeposition along the walls without filling the whole pores was difficult, as indicated by the TEM images, but they were still able to measure electrical transport properties and conclude the metal–semiconductor transition was dependent on the tube wall thickness not diameter.

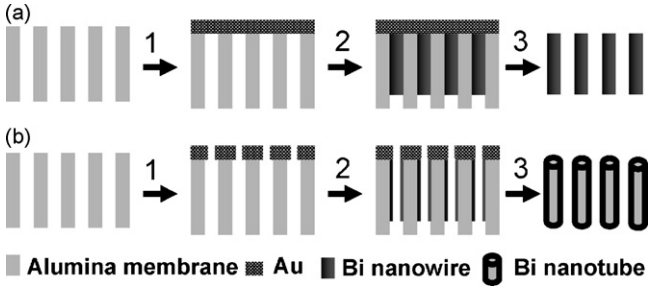

Fig. 5. Schematic illustration of the fabrication processes for Bi nanowires (a) and Bi nanotubes (b). (1) Sputter Au seed layer; (2) electrodeposited Bi nanowires or nanotubes inside the nanochannels; (3) remove Au seed layer and alumina membrane to release Bi nanowires or nanotubes.

2.2. Electrodeposition of $Bi_{1-x}Sb_x$

The bulk properties of $Bi_{1-x}Sb_x$ alloys change dramatically with composition, being semimetals over most of the compositional range except for $0.07 \leq x \leq 0.22$, which are semiconductors with a maximum band gap of about 20 meV. Semiconducting $Bi_{1-x}Sb_x$ alloys are of more interest because they are the best n-type thermoelectric materials around liquid nitrogen temperatures. To date a maximum ZT of ~0.42 for a $Bi_{1-x}Sb_x$ thin films was observed in 18 at.% Sb at 60 K [14,40–42]. Although this is not a competitive ZT value for most applications, one-dimensional nanostructure can further enhance the thermoelectric efficiency, as Dresselhaus and co-workers predicted, with a ZT of 1.25–1.5 for 35–45 nm diameter nanowires of 10–15 at.% Sb [43]. In spite of these calculations, the reports on electrodeposited $Bi_{1-x}Sb_x$ have produced little results in terms of thermoelectric characterization focusing primarily on development of electrolytes. Electrodeposition of these alloys must first address the difference in standard potentials for the reduction of each element. Besse et al. [44] did so with the electrodeposition $Bi_{1-x}Sb_x$ alloys on glassy carbon from electrolytes containing 4 M NaCl, 1 M HCl and various Bi^{3+} and Sb^{3+} concentrations. The addition of NaCl provided a sufficiently high concentration of Cl^- ions in the solutions such that Sb^{3+} formed stable $SbCl_4^-$ complexes, shifting the reduction potential. $Bi_{1-x}Sb_x$ films with a wide range of compositions (x = 0.0–0.8) were deposited by controlling the Bi/Sb ratio in the electrolytes and applied potential or current density. With $-340 \leq E \leq -300$ mV (vs. SCE), or $-10 \leq i \leq -4$ mA/cm^2, the $Bi_{1-x}Sb_x$ films were homogeneous, and adhered well to the substrates. The X-ray diffraction patterns indicated that the as-deposited films were polycrystalline with hexagonal or equivalent rhombohedral alloy phase.

In a similar approach, Vereecken et al. [45] reported the electrodeposition of $Bi_{1-x}Sb_x$ films on evaporated Au wafers from an aqueous solution of $(0.1-y)$ M $BiCl_3$ + y M $SbCl_3$ + 2.4 M HCl + 0.03 M ethylenediaminetetraacetic acid (EDTA) with y ranging from 0 to 0.1 M. EDTA was used as a complexing agent to increase the solubility of Sb. The deposited Sb content depended almost linearly on the Bi/Sb atomic ratio in the solutions. XRD patterns exhibited characteristic (0 1 2) and (0 2 4) peaks for the hexagonal crystal structure of Bi and Sb indicating the polycrystallinity of the films. For all compositions, the as-deposited films were matte gray and exhibited faceted grains. The grain size increased with Sb content and ranged from ~1 μm for pure Bi to several microns for pure Sb films.

Martin-Gonzalez et al. [46] electrodeposited $Bi_{1-x}Sb_x$ films on platinum from a non-aqueous solvent (i.e. dimethyl sulfoxide (DMSO)). DMSO was chosen because of the higher solubility of Sb ions in DMSO. In addition, it has a larger solvent window than water, which allows for the use of a wider range of potentials to tailor the film properties without reduction of the solvent. The electrolytes consisted of $Bi(NO_3)_3 \cdot 5H_2O$ and $SbCl_3$ dissolved in DMSO. They found the film compositions were most sensitive to the concentrations of the Bi and Sb salts. Based on the thin film studies, Stacy's group also electrodeposited 200 nm $Bi_{1-x}Sb_x$ nanowires utilizing anodic alumina membranes as nanotemplates. The obtained $Bi_{1-x}Sb_x$ nanowires were polycrystalline and preferentially oriented along {1 1 0} planes. However, the composition was not homogeneous along the axis of nanowires. During the first 1–2 μm of the nanowires, essentially pure Sb was electrodeposited

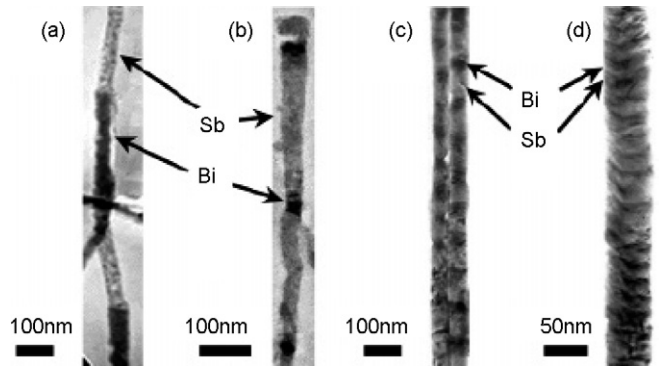

Fig. 6. TEM images of Bi/Sb superlattice nanowires with tunable superlattice periods. Reprinted with permission from ref. [49]. Copyright [2005] American Chemical Society.

followed by 14 at.% Sb. The authors hypothesized that the inhomogeneity of the nanowires might be attributed to change in Bi^{3+}/Sb^{3+} ratio at the surface of the electrode during the early stage of electrodeposition. They also reported the electrodeposition of 40 nm $Bi_{1-x}Sb_x$ nanowires [47].

Li et al. [48] applied their pulse electrodeposition technique to synthesize 40 nm $Bi_{1-x}Sb_x$ nanowires, similar to their prior works on Bi nanowires. They were able to demonstrate single crystal nanowires with a [110] preferred orientation [35–38]. Although direct evidence for the length dependent composition was not demonstrated, the crystallinity and uniform compositions were attributed to uniform metal ion concentrations at the interface due to the steady state concentrations achieved during the rest period. This approach may be a feasible technique to overcome composition variation along nanowire lengths but would require demonstration by more rigorous analysis than XRD.

Alternatively, pulsed plating can be used to create multilayers, a method Xue et al. [49] investigated by electrodepositing Bi/Sb superlattice nanowires from a single bath with stepwise potential pulses. Superlattice configurations are important to nanostructured thermoelectric materials as they have been identified as a means to reduce lattice thermal conductivity by phonon scattering while maintaining electrical conductivity. The electrodeposition was carried out in a two-electrode configuration at 16 °C in ethanol containing 0.01 M $BiCl_3$ + 0.08 M $SbCl_3$ + 0.2 M H_3BO_3 + 0.01 M $C_4H_6O_6$ and 0.1 g/l $CH_3(CH_2)_{11}SO_3Na$. An alumina membrane coated with a Au film on one side was used as the cathode, while a graphite plate was used as the anode. The pH of the electrolytes was adjusted to 2. Two alterative potentials: −0.6 and −1.4 V, were employed to deposit Bi/Sb superlattice structures where the more noble Bi was deposited at a more positive potential than that of Sb. Clear interfaces between Bi and Sb were observed under TEM (Fig. 6). Although, compositional analysis of single components indicated slight codeposition, with 5% Sb in the Bi and 15% Bi in the Sb, this method is a powerful tool for superlattice fabrication, which demonstrates the versatility of electrodeposition techniques.

2.3. Electrodeposition of Bi_2Te_3

Bi_2Te_3 and its alloys are currently the most widely used thermoelectric materials for room temperature applications, and thus one of the most extensively investigated thermoelectric materials by electrodeposition. Bi_2Te_3 is a narrow band gap semiconductor with an E_g = ~0.18 eV at 300 K. Bi_2Te_3 has a rhombohedral structure, which is best described by hexagonal symmetry, and anisotropic thermoelectric properties. The best ZT value occurs along the directions perpendicular to the *c* axis [15,50]. Bi_2Te_3 crystals can be either n- or p-type depending on the doping. Intrinsic doping occurs when there is an excess of Bi (p-type) or excess Te (n-type) in the deposit. The optimum composition for thermoelectric coolers is $Bi_{0.5}Sb_{1.5}Te_3$ (p-type) with ZT ≈ 1 near room temperature [51]. This high ZT has also made them the most thoroughly characterized electrodeposited material for their thermoelectric properties.

Electrodeposition of Bi_2Te_3 has mostly been carried out from acidic nitric baths. Takahashi et al. [52,53] first investigated the electrodeposition of Bi_2Te_3 thin films on Ti sheets, correlating the deposition conditions and film compositions. The electrolytes were made by dissolving Bi_2O and TeO_2 in acidic nitric bath (pH of 0.7–1.0). The Bi_2Te_3 thin films were electrodeposited at −0.25 V vs. Ag/AgCl (3.33 M KCl) within the diffusion limited range from solutions consisting of 1.5 mM $HTeO_2^+$ and various Bi^{3+} concentrations ranging from 0.15 to 2.5 mM. However, the film compositions were far from the stoichiometric and the deposits consisted of a mixture of Te metal and Bi_2Te_3 or BiTe phase. The authors concluded that the film composition was controlled by electrolyte composition. Since Bi^{3+} ion can be easily converted to the hydrolysis product, $Bi(OH)_3$, it was difficult to prepare the electrolytic bath. Thus, they tried to improve the solution stability by adding EDTA as a complexing agent [54]. However, the results obtained were very similar to the ones without EDTA.

Magri et al. [55] and Michel et al. [56,57] later improved the Bi_2Te_3 electrodeposits by controlling the deposition potential/current density and the electrolyte concentration. The electrolytes were made by dissolving $Bi(NO_3)_3$ and tellurium metal in 1 M HNO_3. Based on the electroanalytical studies, Bi_2Te_3 thin films were electrodeposited potentiostatically and galvanostatically on stainless steel [49,50]. For an electrolyte with a Bi/Te ratio equal to 2/3 and 0.02 M $HTeO_2^+$, the film compositions obtained from −150 to −195 mV were always slightly Te-rich compared to the stoichiometric composition. For a solution with a Bi/Te ratio equal to 1, the potential range from −40 to −110 mV gave slightly Te-rich thin films while higher cathodic potentials (−110 to −140 mV) produced slightly Bi-rich deposits. The films composed of Bi_2Te_3 crystal phase had a preferential orientation along the {1 1 0} planes, but this preferred orientation weakened with the increase of Bi content in the deposit [57].

Some of the more seminal work was conducted by Martin-Gonzalez et al. [58], who systematically investigated the electrodeposition of Bi_2Te_3 films from a nitric acid bath. They produced a Pourbaix-type diagram for the electrodeposition of Bi and Te at 25 °C, 1 atm from the solution, which showed the thermodynamic stability of the dominant species as a function of potential and pH (Fig. 7). The diagram indicated that Bi_2Te_3 could be formed directly by the reduction of its cations and was stable over the entire range of pH as a bulk material, at potentials more negative than 0.325 V vs. Ag/AgCl (3 M NaCl). They pointed out there were two mechanisms for the electrodeposition of Te. Between −0.4 and −0.05 V vs. Ag/AgCl, $HTeO_2^+$ ions were directly reduced to Te^0; but between −0.6 and −0.4 V, $HTeO_2^+$ ions were first reduced to gaseous H_2Te followed by immediate transformation to Te^0. They observed that the negative Gibbs free energy of Bi_2Te_3 compound formation shifted the deposition potentials to more positive values compared with the reduction potentials for depositing Bi and Te alone.

Other bismuth telluride thin film studies include Tittes et al. [59] who reported the galvanostatic electrodeposition of Bi_2Te_3 films onto nickel substrates from acidic nitric acid electrolytes. The addition of paper-glue led to bright and adherent deposits up to 15 μm thick. All films exhibited strong {1 1 0} preferential orientation. Only n-type semiconductors were observed under the experimental conditions.

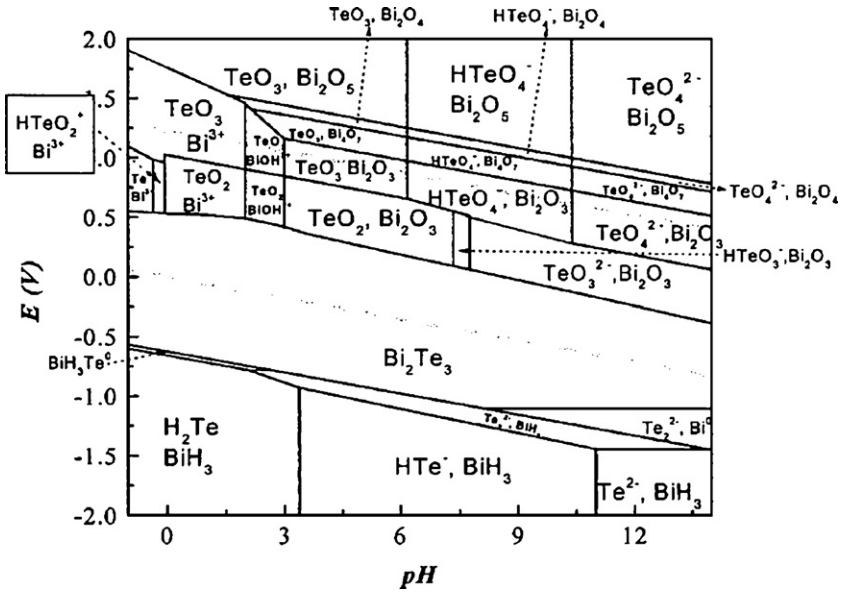

Fig. 7. Pourbaix-type diagram for the electrodeposition of Bi and Te (at 25 °C, 1 atm, and Bi = 0.0075 M and Te = 0.01 M) showing the thermodynamic stability of the dominant species as a function of potential and pH. Reprinted with permission from ref. [58]. Copyright [2002] The Electrochemical Society.

More recently, electrochemical atomic layer epitaxy (ECALE) of Bi_2Te_3 has been investigated by Zhu et al. as an alternative approach to codeposition of Bi and Te [60]. ECALE is a deposition technique utilizing controlled surface reactions, typically underpotential deposition (UPD), and electrolyte cycling to achieve monolayer precision over electrodeposits [61]. Separate solutions are used to deposit each element with rinsing steps between each layer to prevent cross contamination. The process utilized a sputtered Pt working electrode with an automated electrochemical thin-layer flow deposition reactor based on previous designs from Stickney's group [62], with modifications to improve mixing and reduce trapping of bubbles. The Bi electrolytes contained 0.1 mM $Bi(NO_3)_3{\cdot}5H_2O$ + 0.1 M $HClO_4$ with a pH of 1.5. The Te electrolyte consisted of 0.1 mM TeO_2 + 0.1 M $HClO_4$, pH 8.5. The pH of rinsing solutions was set to the same value of the subsequent deposition electrolyte. Bi was controlled by UPD and the Te required an additional reductive stripping step to remove the bulk Te, with only UPD Te remaining [63,64]. The entire process was automated to deposit 200 monolayers, requiring a shift in the UPD for the first 30 monolayers due to the contact potential between the substrate and forming deposit. The Bi_2Te_3 stoichiometry was confirmed with XRD and EDS, however, rough morphology and incomplete stripping of bulk Te led to inhomogeneous deposits. The authors did not report on the transport properties of the film. Improvements to the process were later attempted with a thermally evaporated polycrystalline Au substrate, resulting in more compact films [65].

Despite the valuable contributions from the aforementioned reports on electrodeposited bismuth telluride thin films, they focused solely on synthesis and composition, with little or no data to characterize Seebeck coefficients and thermoelectric figures of merit. Fortunately, more groups have begun characterizing the structure–property relationship in addition to synthesis conditions and mechanisms, creating a more comprehensive picture of these materials.

The work of Miyazaki and Kajitani [66] investigated the influence of deposition potentials on the Seebeck coefficients of Bi_2Te_3 films. They electrodeposited the films on Ti sheets from acidic nitric baths. The films prepared between $+20 \le E \le +60$ mV vs. Ag/AgCl (saturated KCl) exhibited strong (1 1 0) orientation, whereas those prepared between $+60 \le E \le +80$ mV showed (1 0 5) preferred orientation. The films prepared at $E < +20$ mV showed p-type conduction (Bi-rich), while those prepared at $+20 \le E \le +80$ mV showed n-type conduction (Te-rich). The largest Seebeck coefficient of deposits was $-63\ \mu V/K$, which is much smaller than bulk counterparts (i.e. $-250\ \mu V/K$). Lee et al. [67] conducted the similar investigation where they obtained a Seebeck coefficient of $-60\ \mu V/K$. The maximum in-plane power factor ($S^2\sigma$) was $3.5 \times 10^{-4}\ W m^{-1}\ K^{-2}$.

The in-plane power factors, defined as $S^2\sigma$, were reported as a function of applied potential for annealed Bi_2Te_3 electrodeposits from acidic nitric baths by Yoo et al. [68]. Sputtered Bi_2Te_3 thin films on SiO_2/Si substrates were used as working electrodes. By using sputtered Bi_2Te_3 thin films, the lattice mismatch between substrate and deposit could be minimized to reduce defects formation. The sputtered Bi_2Te_3 layer also worked as a buffer layer for the Hall effect measurement of electrodeposited Bi_2Te_3 film onto the substrate. Bi_xTe_y films of 6 μm thick were electrodeposited potentiostatically from −10 to −400 mV vs. SCE and their compositions ranged from 57.0 to 62.4 at.% of Te. The deposited films were then annealed at 250 °C for 2 h in forming gas (7.2% H_2 in Ar) prior to the Seebeck coefficient and Hall effect measurements. They observed that the in-plane Hall mobility decreased with increasing carrier concentration, while the magnitude of the Seebeck coefficient increased with increasing electrical conductivity to the maximum ($-188.5\ \mu V/K$) at the composition of 39.66 at.% Bi and 60.34 at.% Te deposited at −170 mV vs. SCE (Fig. 8). Overall the maximum in-plane power factor of electrodeposited n-type Bi_2Te_3 films after annealing was $12 \times 10^{-4}\ W\ m^{-1}\ K^{-2}$, comparable to the reported $\sim 12 \times 10^{-4}\ W\ m^{-1}\ K^{-2}$ along the *c*-axis direction for bulk Bi_2Te_3 synthesized by a metallurgic process [15].

Li et al. [69] demonstrated the electrodeposition of thick Bi_2Te_3 films (100–500 μm) on a sputtered gold substrate, which is desired for the fabrication of thermoelectric modules applied to larger areas. The Seebeck coefficient of as-deposited Bi_2Te_3 thick film was $-68\ \mu V/K$ before annealing and increased to $-125\ \mu V/K$ after annealed at 300 °C for 2 h in an inert atmosphere.

In addition to acidic nitrate baths, acidic sulfate baths were used to electrodeposit Bi_2Te_3. Heo et al. [70] investigated Bi_2Te_3 electrodeposition in an electrolyte consisting of 2 mM $Bi_2(SO_4)_3$

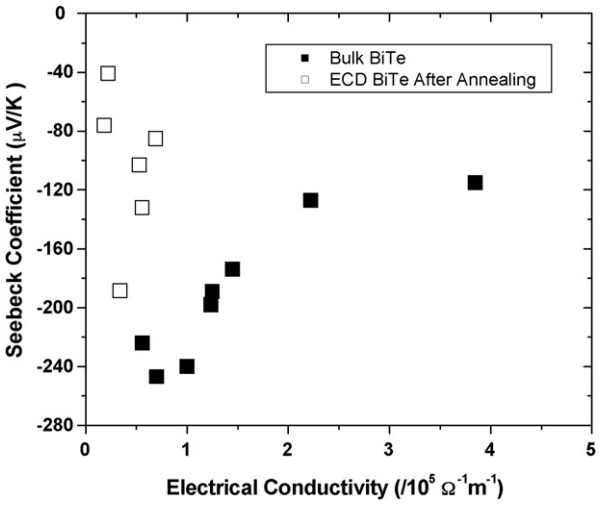

Fig. 8. Dependence of Seebeck coefficient of Bi_xTe_y electrodeposits on electrical conductivity. Reprinted with permission from ref. [68]. Copyright [2005] Elsevier Ltd.

and 2.6 mM K_2TeO_3 in dilute sulfuric acid of pH 0.5. Nearly stoichiometric compositions were obtained at potentials from +30 to −450 mV vs. Ag/AgCl (sat's KCl). The films obtained at potentials more positive than −100 mV exhibited a smooth and uniform light-gray surface, while the films obtained at potentials more negative than −100 mV had a rough, black surface with very poor electrical conductivity. Films deposited at +25 mV and 0 V showed strong {1 1 0} preferential orientation. With the increase in the cathodic potential, the {1 1 0} crystal orientation weakened. Such an orientation trend is very similar to that in acidic nitric baths. The Seebeck coefficients of as-deposited films were around −100 μV/K independent of deposition potentials. The electrical conductivity, however, decreased with increasing cathodic potential and reached the maximum of ~670 S/cm at 0 mV. The highest power factor ($S^2\sigma$) of 7.4×10^{-4} W m^{-1} K^{-2} at 293 K was obtained at 0 mV, which is much lower than the bulk value along *c*-axis.

Bi_2Te_3 nanowires have been almost exclusively electrodeposited by template-directed techniques, and in most cases using the deposition conditions from thin film investigations. The applied potentials have been shown to depend upon the electrolyte concentration and material of the seed layer. Sapp et al. [71] first reported the galvanostatic electrodeposition of Bi_2Te_3 nanowires into an anodic alumina membrane (200 nm). As-deposited nanowires were polycrystalline with no obvious preferential orientation.

Prieto et al. [72] and Sander et al. [73,74] investigated the potentiostatic electrodeposition of Bi_2Te_3 nanowires. The nanotemplates used were in-house fabricated alumina membranes with average pore diameters of 25, 45 and 75 nm, a porosity of ~50%, and a thickness of ~60 μm. Approximately, 1 μm thick Ag was sputtered on side of the membrane as the working electrode. The nanowires were deposited at −0.46 V vs. Hg/$HgSO_4$ (sat K_2SO_4). Approximately, 80% of the pores were filled by Bi_2Te_3 nanowires. The nanowire composition remained constant along the nanowire. They also found that the nanowire texture depended on the pore diameter. For the larger diameter nanowires (>45 nm), the deposited nanowires were highly oriented with the {1 1 0} planes perpendicular to the wire axis. For the 25 nm nanowires, both (1 1 0) and (3 0 0) peaks were strong.

Li's group also [75] reported the galvanostatic electrodeposition of ~50 nm Bi_2Te_3 nanowires. These single crystalline nanowires were highly oriented with the {1 1 0} planes perpendicular to the wire axis. Approximately, 100% of the pores were filled by Bi_2Te_3 nanowires probably due to the better quality of alumina template than previously reported.

A more thorough investigation on the influence of mass transport on electrodeposition of Bi_2Te_3 nanowires into alumina templates (thickness of ~60 μm and pore diameter of ~200 nm) was conducted by Wang et al. [76] by means of a rotating disk electrode. The nanowires were deposited potentiostatically and the rotation rate varied from 400 to 1400 rpm. They found that mass transport of electrolytes into alumina templates of high aspect ratio played a significant role in determining the composition of nanowires. The composition gradient along the nanowires was about 0.17 at.% per micron at −0.14 V vs. SCE at 400 rpm, and doubled at −0.3 V and 400 rpm. Increase of the diffusion rate increased Bi content in the nanowires.

Zhang's group [77] extended their pulse electrodeposition method to the fabrication of Bi_2Te_3 nanowires with anodized alumina. The pulse on-time was 3 ms and pulse off-time was 10 ms. As-deposited Bi_2Te_3 nanowires were highly oriented with {0 1 5} planes along the growth direction. The composition was close to the stoichiometric composition. They measured the variation of electrical resistance of 40 and 60 nm Bi_2Te_3 nanowires, respectively, as a function of temperature from 290 to 320 K. The electrical resistances decreased with temperature, and exhibited a negative temperature coefficient of resistance (TCR), i.e. a typical semiconductor-like characteristic. The TCRs were -1.25×10^{-4} and -2.16×10^{-3} K^{-1} for 40 and 60 nm nanowires, respectively. The TCR of 40 nm nanowires was much smaller than that of 60 nm nanowires, indicating that the nanowires with smaller diameter had lower resistance sensitivity to temperature.

An interesting hybrid inorganic/organic nanostructure has also been synthesized with bismuth telluride. Xu et al. [78] demonstrated the synthesis of core/shell polyaniline/Bi_2Te_3 nanowires by template-directed electrodeposition. First, they electrodeposited polyaniline nanotubes inside the pores of anodized alumina followed by electrodeposition of Bi_2Te_3 cores within the nanotubes. Wang et al. [79] also reported the Seebeck coefficient of electrodeposited Bi_2Te_3 nanowires from acidic nitrate baths. The maximum Seebeck coefficient of 270 μV/K was observed for 50 nm nanowires at 306 K, which is higher than that of bulk Bi_2Te_3. Unfortunately, they found an increase in resistance of the nanowires, above that of bulk values, which was probably due to the polycrystalline structure of their wires or even contact resistance. Although, Wang and co-workers did report the thermopower of Bi_2Te_3 nanowires, these nanowires were in the template making it impossible to accurately measure the ZT.

In perhaps one of the most stringent attempts to characterize the thermoelectric properties of template-directed electrodeposited nanowires, Zhou et al. [80] illustrates the difficulty of this task. Their setup required suspending a single nanowire across two heater membranes suspended in air and contacting the wire with two focused ion beam written Pt electrodes. This configuration allowed them to make S measurements and four more contacts were made for the remaining measurements. The nanowires, taken from the work Jin et al., were intrinsically p-type and single crystalline with a growth direction perpendicular to the *c* axis. Their measurements found S increase over the bulk value for $Bi_{0.46}Te_{0.54}$ and decreased compared to the bulk for $Bi_{0.56}Te_{0.44}$. The electrical conductivity was near bulk values and the lattice thermal conductivity was shown to decrease at temperatures below 300 K.

Finally, Menke et al. [81,82] reported the ZT values of Bi_2Te_3 nanowires using alternative electrodeposition technique. Instead of using a porous membrane as scaffold to fabricate Bi_2Te_3 nanowires, they synthesized the nanowires by the step edge selective electrodeposition on highly oriented pyrolytic graphite (HOPG) surfaces (Fig. 9b). The applied potential program (Fig. 9a), referred

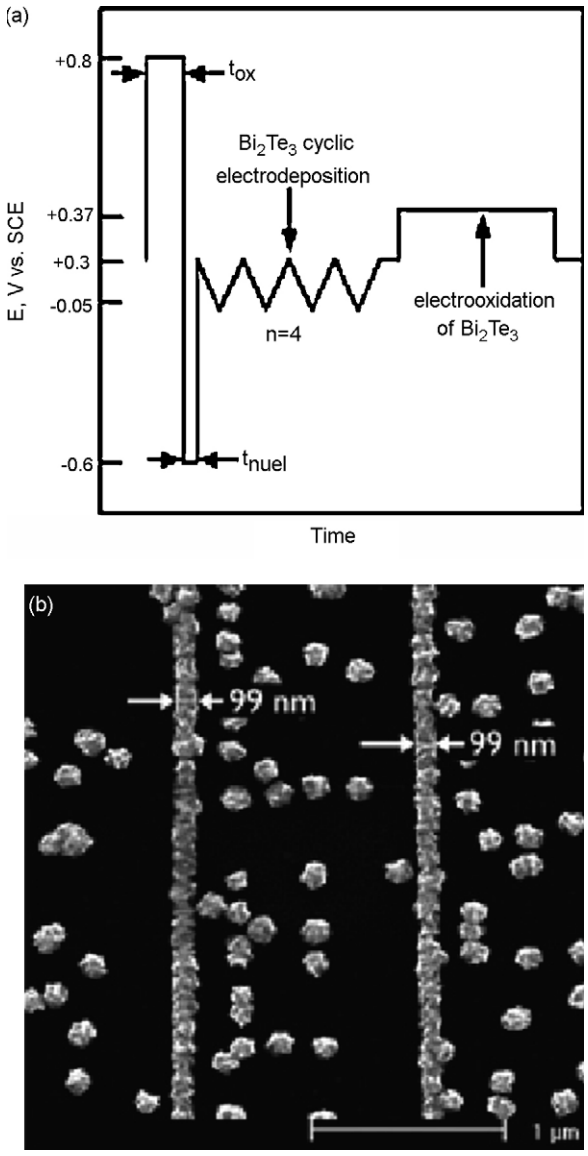

Fig. 9. (a) Potential program used for the synthesis and electrooxidation of Bi_2Te_3 nanowires on HOPG electrodes; (b) a typical SEM image of ~100 nm Bi_2Te_3 nanowires. Reprinted with permission from ref. [81]. Copyright [2006] American Chemical Society.

to as cyclic electrodeposition/stripping, consisted of three steps: (1) mild oxidation of the basal plane step edges on a piece of HOPG at +0.80 V (vs. SCE) for 5 s; (2) nucleation of Bi_2Te_3 nanoparticles along the oxidized step edges at −0.60 V for 5 ms; (3) co-deposition of Bi_2Te_3 and excess bismuth during a cathodic potential scan from +0.3 to −0.05 V, and subsequent stripping of excess bismuth during a anodic potential scan from −0.05 to +0.30 V, producing stoichiometric Bi_2Te_3 deposits. Step 3 was repeated until the Bi_2Te_3 nanoparticles grew to coalesce forming continuous Bi_2Te_3 nanowires. Using this method, they prepared randomly oriented polycrystalline Bi_2Te_3 nanowires up to 1 mm long. The diameter of the nanowires was controlled by the number of electrodeposition/stripping cycles. At 10 cycles, the diameter was about 100 nm, which was the smallest diameter achievable using this process. Using the Harman method, they measured the ZT values of 200 nm Bi_2Te_3 nanowires deposited at 20 cycles. The highest ZT measured was 0.82. They also observed that the measured ZT decayed from 0.82 to nearly zero after the nanowires exposed in air for 2 days. The oxide formation on the nanowire surface was responsible for this decay, thus indicating the challenge with single wire characterization methods.

2.4. Electrodeposition of Sb_2Te_3 and $(Bi_{1-x}Sb_x)_2Te_3$

Antimony telluride (Sb_2Te_3) has the same crystal structure as Bi_2Te_3 with Sb atoms occupying Bi lattice sites. Sb_2Te_3 also acts as a p-type dopant in Bi_2Te_3 to form p-type $(Bi_{1-x}Sb_x)_2Te_3$ solid solution. However, electrodeposition of Sb_2Te_3 or $(Bi_{1-x}Sb_x)_2Te_3$ is challenging since it is difficult to achieve a sufficiently high concentration of Sb in an aqueous solution. This obstacle has limited the work on these materials primarily to synthesis.

Electrodeposition of Sb_2Te_3 thin films on an indium tin oxide (ITO) substrate was reported by Leimkuhler et al. [83]. The solutions consisted of 0.08–0.16 mM $SbCl_3$, 0.2 mM TeO_2, 0.5 M KCl, 100 mL/L phthalate buffer solution (pH 4), with unknown amount of HCl. The solution pH was adjusted to 4.25 by adding KOH and temperature was kept at 368 K. Stoichiometric Sb_2Te_3 was obtained between −600 and −750 mV vs. Ag/AgCl (sat'd KCl) independent of the Sb/Te ratio. As the concentration of Sb ions in the electrolytes increased, more positive potentials were applied to obtain Sb_2Te_3. Thin films deposited had mirror like appearance up to 500 nm, whereas thicker films became dull.

Wang et al. [84] electrodeposited Sb_2Te_3 thin films on highly doped single crystal p-type Si(1 0 0) (4–10 Ω cm). The on-set deposition potential for Sb_2Te_3 on Si(1 0 0) was more negative than −1 V vs. Ag/AgCl (3 M KCl) due to the lower conductance compared to a metal.

The ECALE approach was investigated by Yang et al. for electrodeposition of Sb_2Te_3 [85]. The system consisted of an automated electrochemical thin-layer flow deposition reactor previously mentioned and a sputtered Pt film working electrode. A 0.05 mM Sb_2O_3 solution with a pH of 1.5 and 0.4 mM TeO_2 solution with a pH of 2 were used for Sb and Te deposition, respectively. The UPD for Sb and Te were determined from cyclic voltammograms. These UPDs were used to form a 400 cycle Sb_2Te_3 deposit verified by XRD. The grain size was 20 nm and the optical band gap of the deposit was determined to be 0.42 eV.

Del Frari et al. [86] electrodeposited $(Bi_{1-x}Sb_x)_2Te_3$ thin films from acidic perchloric (1 M) baths with tartaric acid (0.1 M) as a complexing agent. They first conducted the electroanalytical studies of Bi_2Te_3, Sb_2Te_3 and $(Bi_{1-x}Sb_x)_2Te_3$ using a platinum disc as a working electrode. Based on the electroanalytical studies, $(Bi_{1-x}Sb_x)_2Te_3$ thin films were electrodeposited on stainless steel at potentials selected from voltammograms. The influence of the deposition potential on deposit composition was studied in a solution containing 0.01 M $HTeO_2^+$, 0.0025 M Bi^{3+}, 0.0075 M SbO^+, 0.1 M tartaric acid, and 1 M $HClO_4$. From 0 to −0.05 V (vs. SCE), the film compositions were nearly $BiTe_4$, but the XRD studies indicated the presence of Bi_2Te_3 and Te^0. From −0.05 to −0.15 V, $Bi_xSb_yTe_z$ compound with an excess of tellurium was deposited. XRD analysis confirmed the presence of Te^0. The ratio $Bi_xSb_yTe_z/Te^0$ depended strongly on the applied potential. Finally, from −0.15 to −0.3 V, $Bi_{0.5}Sb_{1.5}Te_3$ was deposited independent of the applied potential. They also investigated the influence of $[SbO^+]/[Bi^{3+}]$ ratio on the film composition. The deposition potential was fixed at −0.17 V vs. SCE. When $[SbO^+]/[Bi^{3+}]$ ratio varying from 2 to 6 with a constant $([Bi^{3+}]+[SbO^+])/[HTeO_2^+]$ ratio equal to 1, all films had a $(Bi_{1-x}Sb_x)_2Te_3$ structure; but the antimony and bismuth percentages in the films depended linearly on $[SbO^+]/[Bi^{3+}]$ ratio in solution. An electrolyte containing 11.6 at.% Bi^{3+} ions lead to films with 10 at.% deposited Bi content. Although the authors were able to achieve a good control of the film composition, the compactness and roughness of as-deposited films were not satisfactory. One year

later, they reported pulse electrodeposition of $(Bi_{1-x}Sb_x)_2Te_3$ films to improve the compactness and roughness [87]. Thermoelectric power factors were measured to determine the effect of pulse plating parameters. After annealing at 200 °C in an argon atmosphere for 1 h, films showed a Seebeck coefficient of ~180 μV K^{-1}; the electrical conductivity increased with decrease in t_{on} which might be attributed to more dense deposit. As a result, when t_{on} was in the range of 3–4 s, pulse plated films show a high power factor of ~600 μW K^{-2} m^{-1}. When the t_{on} was fixed at 5 s, the power factor was decreased to ~100 μW K^{-2} m^{-1} and further decreased to ~50 μW K^{-2} m^{-1} as the t_{on} increased to 9 s.

Martin-Gonzalez et al. [88] reported an electrolyte using tartaric acid as a complexing agent to increase the Sb solubility in water by forming Sb-tartaric complexes. The composition of the solution was 0.01 M $HTeO_2^+$, 0.0019 M Bi^{3+}, 0.0056 M SbO^+, 0.84 M tartaric acid and 1 M HNO_3. To study the electrodeposition of $(Bi_{1-x}Sb_x)_2Te_3$, they compared the cyclic voltammograms for solutions with and without Sb plus tartaric acid. Their shapes were independent of the presence of Sb except that the reduction potential was shifted ~100 mV more cathodic upon the addition of Sb-tartaric complex, which is consistent with the fact that complexed cations are generally reduced at more negative potentials than uncomplexed cations. Based on the voltammograms, they concluded that the electrodeposition mechanism of $(Bi_{1-x}Sb_x)_2Te_3$ was similar to that of Bi_2Te_3. The deposition took place first by electrochemically reduction of $HTeO_2^+$ to Te^0, followed by under potential deposition (UPD) of Bi and Sb to form the compound. These studies [88] were also used to successfully fabricated $(Bi_{1-x}Sb_x)_2Te_3$ nanowires using anodized alumina as scaffolds. The EDAX compositions were $Bi_{0.7}Sb_{1.4}Te_{2.9}$ for 200 nm and $Bi_{0.6}Sb_{1.6}Te_{2.8}$ for 40 nm, respectively, with approximately 80% of the pores filled with nanowires.

Jin et al. [89] later electrodeposited Sb_2Te_3 nanowires from an acidic nitrate bath with citric acid as a complexing agent. The Sb_2Te_3 nanowires were galvanostatically deposited and close to 100% of the nanopores were filled with the nanowires. In addition, as-deposited nanowires grew highly preferentially along {1 1 $\bar{2}$ 0} planes.

Xiao et al. [90] reported the potentiostatic electrodeposition of $(Bi_{1-x}Sb_x)_2Te_3$ from acidic tartaric-nitric baths. The effect of solution concentration on film composition was investigated by varying Bi^{3+} concentration from 0.1 to 0.5 mM while maintaining $HTeO_2^+$, SbO^+, tartaric acid, and nitric acid concentration at 0.7 mM, 1.6 mM, 33 mM and 1 M, respectively. Uniform and compact $(Bi_{1-x}Sb_x)_2Te_3$ films with a wide range of composition were deposited by controlling deposition potentials and solution concentrations. Based on the investigation of thin film deposition, a facile fabrication technique [91] was developed to synthesize superlattice $Bi_2Te_3/(Bi_{0.3}Sb_{0.7})_2Te_3$ nanowires (Fig. 10) from a single bath containing 0.1 mM Bi^{3+}. In this method, a waveform potential profile was applied alternating between −20 and −100 mV vs. SCE.

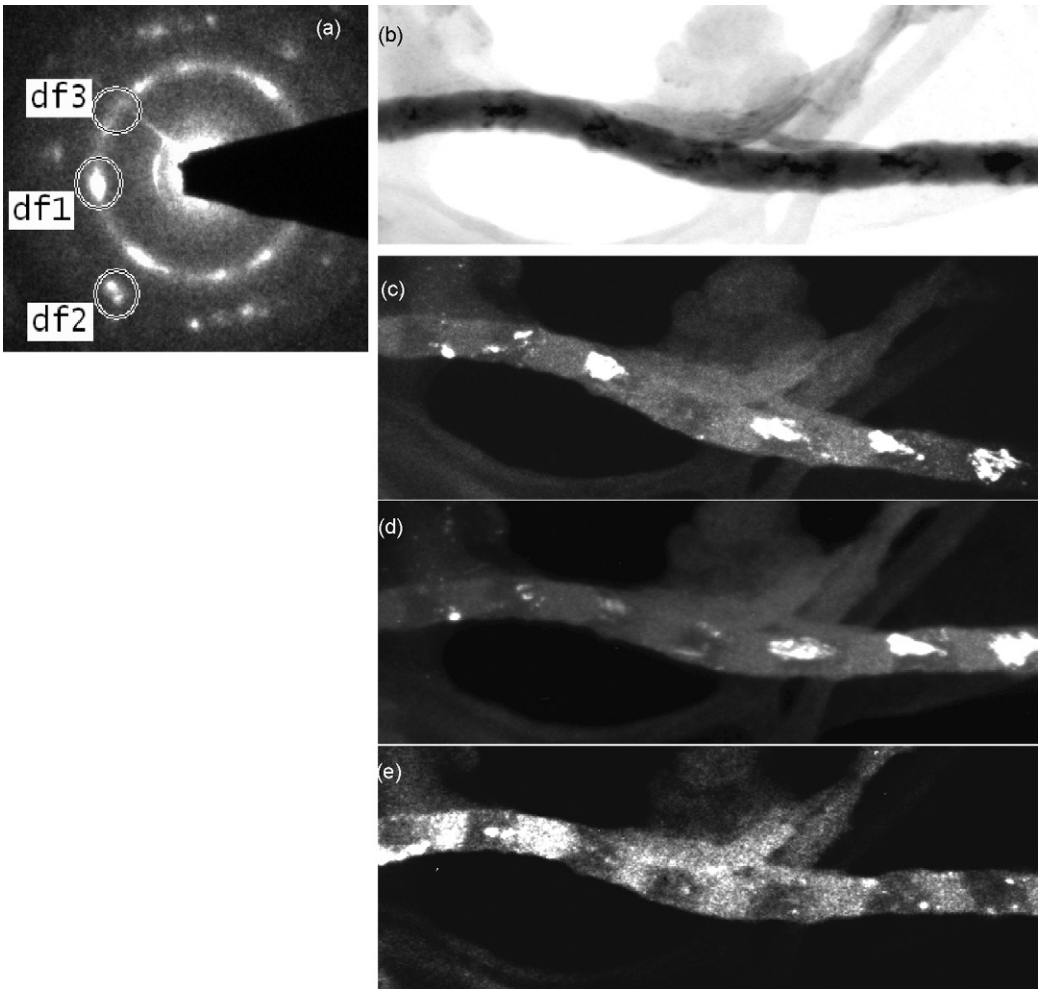

Fig. 10. Electron diffraction patterns and TEM images of superlattice BiSbTe nanowire. Dark field TEM images which correspond to each parts in diffraction patterns are shown from (c) to (e), respectively; image (c) corresponds to df1; image (d) corresponds to df2; image (e) corresponds to df3.

At −20 mV, Bi_2Te_3 with small amount of Sb incorporation (<3 at.%) was deposited; at −100 mV, $(Bi_{0.3}Sb_{0.7})_2Te_3$ was obtained which was very close to the best bulk composition for $(Bi_{1-x}Sb_x)_2Te_3$. The composition and length of each segment were precisely controlled by adjusting deposition potentials and time, which is important in tuning the thermoelectric properties of these nanowires [6].

2.5. Electrodeposition of Bi_2Se_3 and $Bi_2Te_{3-y}Se_y$

Bismuth selenide (Bi_2Se_3) has a similar crystal structure as Bi_2Te_3 with Se atoms occupying Te lattice sites. Bi_2Se_3 is usually used as a dopant in Bi_2Te_3 to form $Bi_2Te_{3-y}Se_y$ solid solution. While Bi_2Se_3 and $Bi_2Te_{3-y}Se_y$ are an important class of thermoelectric materials, most characterization work has been conducted using alternate synthesis techniques, with the work presented here focusing solely on synthesis.

Using an approach similar to electrodeposition of Bi_2Te_3, Torane et al. [92] electrodeposited Bi_2Se_3 from an acidic nitrate bath. The electrolyte was made by first dissolving $Bi(NO_3)_3$ and SeO_2 in concentrated nitric acid and followed by proper dilution to desired concentration. A high quality Bi_2Se_3 film was deposited potentiostatically on stainless steel at −0.09 V (vs. SCE) from a solution containing 0.025 M Bi^{3+} and 0.025 M Se^{2-}. The nitric acid concentration or pH value of the solution was not reported. The as-deposited films were polycrystalline with random orientation. After being annealed at 200 °C in a nitrogen atmosphere for 2 h, the film became preferentially oriented along {0 0 6} planes. They also studied the optical absorption spectrum of as-deposited Bi_2Se_3 thin film. Based on the absorbance variation with wavelength, they calculated the direct band gap energy to be 0.55 eV. This band gap was higher than the bulk value 0.35 eV. The cause of the difference was not given in the report.

Desai [93] electrodeposited Bi_2Se_3 from an aqueous alkaline bath using sodium selenosulfite (Na_2SeSO_3) as the selenide ion source and bismuth nitrate as the Bi^{3+} source. TEA was used as a complexing agent. The electrolyte composition was not reported. The electrodeposition was carried out galvanostatically at $-0.25\ mA/cm^2$ on Ti or stainless steel. The as-deposited thin films were polycrystalline with random orientation. They also reported the band gap energy of 0.57 eV for the as-deposited thin films.

Michel et al. [94] potentiostatically electrodeposited $Bi_2Te_{3-y}Se_y$ thin films from 10 mM $Bi(NO_3)_3{\cdot}5H_2O$ + 4.2–6.5 mM $HTeO_2^+$ + 0.14–0.38 mM Na_2SeO_3 + *X* M HNO_3 (pH 0). At a deposition potential of −55 mV vs. SCE, $Bi_{1.97}Te_{2.67}Se_{0.36}$ thin films were electrodeposited. The as-deposited thin films consisted of crystallites in roughly circular nodules with an average size of 1 μm. The surface roughness (root mean square roughness) was approximately 90 nm.

Martin-Gonzalez et al. [95] reported the electrodeposition of $Bi_2Te_{3-y}Se_y$ nanowires from acidic nitrate baths. The electrolyte consisted of 7.5 mM Bi^{3+}, 9.0 mM $HTeO_2^+$ and 1 mM H_2SeO_3 in 1 M HNO_3. Before synthesizing nanowires, they first investigated the electrodeposition of $Bi_2Te_{3-y}Se_y$ thin film using cyclic voltammetry. They found that the deposition mechanism for $Bi_2Te_{3-y}Se_y$ was different from the mechanism for Bi_2Te_3. For example, $Te_{1-x}Se$ alloys were initially formed instead of elemental Te prior to compound formation. The reduction potential also shifted ∼100 mV more positive. $Bi_2Te_{2.5}Se_{0.5}$ nanowires were potentiostatically electrodeposited at 0 V vs. Ag/AgCl (3 M NaCl) using anodized alumina as scaffolds. More than 85% of the pores were filled with nanowires. The as-deposited nanowires were polycrystalline and grew preferentially with {1 1 0} planes parallel to the Pt seed layer.

The effect of substrate on the electrodeposition of $Bi_2Te_{3-y}Se_y$ thin films was investigated by Bu et al. [96]. The electrolyte consisted of 0.01 M Bi^{3+}, 0.0103 M $HTeO_2^+$, and various H_2SeO_3 concentrations in 1 M HNO_3. They found that deposited Se content increased almost linearly with the increase of H_2SeO_3 concentration in the solutions. At 0.001 M H_2SeO_3, the film had the composition of $Bi_2Te_{2.7}Se_{0.3}$. The as-deposited films on stainless steel and gold substrates, having similar XRD patterns, were randomly oriented polycrystalline. However, the films deposited on the gold substrate had a more compact structure and smaller grain size than the film on stainless steel.

2.6. Electrodeposition of PbTe

Lead telluride, PbTe, is a small band gap semiconductor (about 0.32 eV at 300 K) which has a rocksalt structure (face-centered cubic (FCC)) and belongs to the $Fm\bar{3}m$ space group [97]. PbTe can be either n- or p-type semiconductors as a result of its departure from stoichiometry (Pb-rich PbTe is n-type, while Te-rich PbTe is p-type semiconductor) [98]. PbTe and its derivative compounds are among the most efficient materials for thermoelectric power generators working between 500 and 600 K, making them ideal for harvesting waste thermal energy [99]. Nevertheless, the relatively recent progress on electrodeposition of PbTe has again hindered thermoelectric characterization.

Potentiostatic electrodeposition of PbTe thin films was first reported by Saloniemi et al. [100] for aqueous alkaline solutions of $Pb(CH_3COO)_2$ and TeO_2 with EDTA (disodium salt of ethylendiaminetetraacetic acid) as the complexing agent. The effect of deposition potential on the film composition was studied. They observed that smooth, dense Te-rich PbTe thin films were electrodeposited on Cu and indium tin oxide (ITO) substrates. The X-ray diffraction pattern indicated the PbTe thin film had [2 0 0] preferred crystal orientation. The mechanism of the electrodeposition of PbTe films was studied by electrochemical quartz crystal microbalance (EQCM) [101]. The deposition of PbTe occurred by an induced codeposition mechanism where the initial deposition of Te induced the UPD of Pb.

Epitaxial electrodeposition of PbTe thin films was investigated by Beaunier et al. [102] using (1 1 1) InP single crystal substrates and an acidic nitrate bath. The electrolyte consisted of 0.05 M $Pb(NO_3)_2$ and 0.001 M TeO_2 in 0.1 M HNO_3 with and without 0.5 M Cd^{2+}. The deposition potential, without optimization, was fixed at −0.75 V vs. saturated sulfate electrode (SSE). The as-deposited PbTe films on (1 1 1) InP had poor epitaxy due to the high polycrystallinity. In their work, they also investigated the effect of Cd^{2+} on the morphology of PbTe films. When 0.5 M $Cd(NO_3)_2$ was added to electrolytes, the film morphology was altered from dendritic growth to relatively homogenous dense growth.

Ivanova et al. [103] investigated the potentiostatic electrodeposition of PbTe films onto n-Si(1 0 0) wafers from a solution of 0.05 M $Pb(NO_3)_2$, 0.001 M TeO_2 and 0.1 M HNO_3. The deposition potential was fixed at −0.38 V vs. Ag/AgCl. The nucleation and growth mode of PbTe was determined to be 3D progressive nucleation under the diffusion control. X-ray diffraction patterns indicated PbTe thin film had [2 0 0] preferred crystal orientation.

Myung's group [104] conducted a systematic study of the electrodeposition of PbTe to investigate the effect of electrodeposition conditions on film composition, crystallographic structure, and texture in an acidic nitrate bath. They also reported the growth of single crystalline PbTe cubes (Fig. 11) for the first time [105]. The electrolytes consisted of TeO_2, $Pb(NO_3)_2$ and 1 M HNO_3. The electroanalytical studies of PbTe thin films indicated UPD of Pb onto the overpotentially deposited Te atoms on a substrate. The UPD of Pb was initiated at ∼−0.11 V vs. Ag/AgCl (4 M KCl). The microstructure, composition and preferred growth orientation of PbTe thin films strongly depended on the applied potential and electrolyte concentration. At −0.12 V, the film was granular, dense, and prefer-

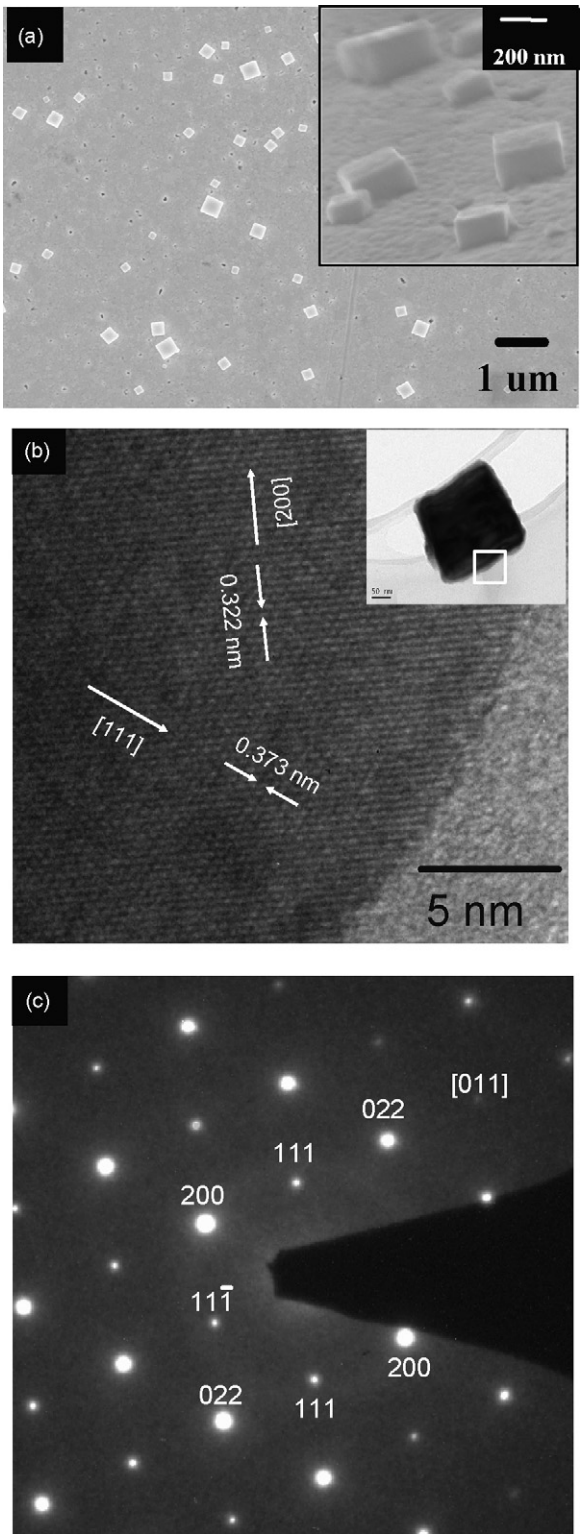

Fig. 11. (a) SEM micrographs of PbTe deposits after 2 min depositions at −0.12 V vs. Ag/AgCl. The inset images provide tilted view at higher magnification. (b) The corresponding HRTEM image of the single crystalline PbTe deposit, obtained after tilting the crystal from horizontal orientation in order to attain relatively thin edges transparent to the electron beam. (c) ⟨0 1 1⟩ zone axis electron diffraction pattern of the PbTe deposit. Reprinted with permission from ref. [105]. Copyright [2007] American Chemical Society.

entially oriented in the [1 0 0] direction. At potentials more negative than −0.15 V, the film was dendritic and preferentially oriented in the [2 1 1] direction. A smooth, compact and polycrystalline film with nearly stoichiometric composition was electrodeposited at −0.12 V on an evaporated polycrystalline Au substrate from a solution containing 0.01 M $HTeO_2^+$, 0.05 Pb^{2+} and 1 M HNO_3. When the concentration of $HTeO_2^+$ was reduced to 0.1 mM, single crystalline PbTe cubes were deposited at the same deposition potential of −0.12 V. It is believed that single crystals of PbTe were preferentially nucleated on Au {1 0 0} plane, which cause the lowest mismatch with the {1 0 0} face of PbTe. After nucleation, the growth of nuclei proceeded with laterally expanding new planes from the top corners of cubes, which was the ⟨1 1 0⟩ direction of PbTe single crystals.

2.7. Electrodeposition of PbSe and $PbSe_{1-x}Te_x$

Similar to PbTe, both PbSe and $PbSe_{1-x}Te_x$ have a rock-salt cubic structure; and an excess of Pb leads to n-type semiconductors and excess of chalcogenide (Se, Te) elements cause p-type semiconductors [106].

To the best of our knowledge Molin and Dikusar [107] were the first to electrodeposit PbSe thin films. They used a solution containing $Pb(CH_3COO)_2$, H_2SeO_3, complexing agents EDTA and CH_3COOH, and supporting electrolyte $NaClO_4$ (pH 3.4). The concentration ratio [Se]/[Pb] was within the range of 0.2–2. The XRD patterns indicated the presence of high quantities of elementary Se in the deposit. Interestingly, the authors found that the electrodeposition of PbSe took place by UPD of Se onto initially deposited Pb on the substrate.

Saloniemi et al. [108,109] later improved the deposition conditions based on Molin's work. Their electrolytes contained 0.001 M SeO_2, 0.1 or 0.01 M $Pb(CH_3CO_2)_2$ and 0.13 or 0.013 M EDTA. The working electrodes were SnO_2 coated glass substrates. Nearly stoichiometric, smooth, mirror-like PbSe films were obtained at potential range of −0.6 to −0.8 V vs. SCE when the concentration ratio [Se]/[Pb] was 0.1, and of −0.4 to −0.75 V vs. SCE when the concentration ratio [Se]/[Pb] was 0.01. The electrochemical reactions involved in the electrodeposition of PbSe were studied by combined EQCM and CV. They confirmed that the electrodeposition of PbSe within these potential ranges took place by an induced codeposition mechanism via a six-electron reduction reaction. Se(IV) was reduce to Se^0 and H_2Se at the same time. Therefore, two different reactions were involved for the electrodeposition of PbSe. One was that Pb^{2+} reacted with Se^0 first deposited on the substrate; the other one was that Pb^{2+} reacted with H_2Se (aqueous) adsorbed on the electrode surface.

A full investigation of PbSe electrodeposition from acidic nitrate solutions was carried out by Streltsov et al. [110] with a solution containing $Pb(NO_3)_2$ and SeO_2 in 0.1 M HNO_3. They also found the deposition of PbSe took place by an induced codeposition mechanism in the potential range of −0.1 to −0.4 V vs. Ag/AgCl (sat'd KCl), where the initial deposition of Se induced the underpotential reduction of Pb. Only a minor alteration was observed in the film composition in this potential range. This range overlaps very well with that for PbTe electrodeposition in an acidic nitrate bath. Slightly Se-rich PbSe films were deposited onto platinum substrates without preferential orientation. The presence of high concentration of Cd^{2+} in the electrolyte greatly influenced the film orientation, grain size and surface morphology [111]. PbSe films deposited at −0.3 V from a solution containing 1 M Cd^{2+} exhibited a smoother surface and strong [2 0 0] preferential orientation. As the Cd^{2+} concentration increased from 0 to 1.4 M, the average PbSe grain size increased from ~45 to ~70 nm. The authors also investigated the photoelectrochemical deposition of PbSe films onto

p-Si(1 0 0) wafers (40 Ω cm) [112,113]. In the darkness, Se could not be deposited alone on silicon while Pb could be over-potentially deposited alone at potentials more negative than −0.4 V. Thus, UPD of PbSe could not occur on Si substrate in the darkness. Under illumination, however, the onset deposition potential for Se was ∼0 V. In both dark and illuminated conditions, only PbSe nanoparticles (40–200 nm average size) were deposited onto p-Si(1 0 0) wafers rather than continuous films.

In related studies, Froment and co-workers [114–116] investigated the epitaxial electrodeposition of PbSe on single crystal InP(1 1 1). The electrolyte consisted of 0.05 M $Pb(NO_3)_2$, 0.001 M SeO_2 and 0.1 M HNO_3 with various $Cd(NO_3)_2$ concentration. To achieve a good epitaxial growth, the Cd^{2+} concentration had to be around 0.5 M and the cathodic potential had to be maintained within the range of −0.7 to −0.75 V vs. SSE. The epitaxial grown PbSe thin films had the same crystal orientation as InP(1 1 1). The highest epitaxial thickness reported was 180 nm. The adsorption of Cd^{2+} on the electrode surface provided a strong inhibiting effect on the UPD of PbSe which favored the epitaxial growth. However, Cd was incorporated between the InP and PbSe interface (2–4 at.%) and in the bulk of the PbSe layers (1 at.%). They revealed that an epitaxial CdSe film was formed on InP(1 1 1) before PbSe growth during the first steps of electrodeposition. The Cd content in the bulk PbSe was quite low compared to the surface of InP in spite of a continuous adsorption of Cd^{2+} during the PbSe electrodeposition.

Stickney and co-workers studied ECALE of both PbSe thin films and PbSe/PbTe superlattices [117,118]. The solution for Pb deposition was 0.2 mM $Pb(ClO_4)_2$ and 0.1 M $NaClO_4$ buffered to pH 5.5 with 50 mM $CH_3COONa{\cdot}3H_2O$, and 0.2 mM SeO_2 and 0.1 M $NaClO_4$ also buffered to pH 5.5 with 50 mM $CH_3COONa{\cdot}3H_2O$ for Se deposition. A thermally evaporated Au film at 400 °C with a Ti adhesion layer with stringent handling procedures was used as the substrate. While Pb was deposited at an underpotential, Se was deposited at an overpotential that could be controlled using low deposition times. The UPD shift shown in the first 20 cycles was attributed to the changing electronic structure from the gold substrate to the deposited semiconductor. A 50 cycle run produced a 22 nm thick PbSe sample showing a 1:1 stoichiometry by electron probe microanalysis and a polycrystalline structure with a predominate (2 0 0) orientation by XRD. Absorption spectra also indicated a four-fold increase in the band gap from bulk values. Stickney's later work with PbSe/PbTe superlattices utilized the same solutions with the addition of a Te solution containing a 0.2 mM TeO_2 and 0.1 M $NaClO_4$ buffered to pH 9.2 with 50 mM $CH_3COONa{\cdot}3H_2O$. The deposit consisted of a 4:4 PbSe/PbTe superlattice with a total of 81 periods confirmed by XRD.

In a study reported by Hens et al. [119], the electrical and optical properties were correlated to the size and shape of PbSe nanocrystals on single crystalline Au(1 1 1). The solution contained 2.5 mM $Pb(CH_3CO_2)_2$, 1.25 mM SeO_2, 3 mM EDTA, and 0.7 M acetic acid. The applied potential varied from −600 to −700 mV vs. SCE. The as-deposited PbSe nanocrystals had a thickness of ∼5 nm and lateral thickness of 15–20 nm. The electrodeposition occurred by a two-dimensional nucleation and growth mechanism. The nanocrystals were oriented with {2 0 0} planes parallel to Au(1 1 1) surface. Quantum confinement was effective in the direction perpendicular to the gold surface, leading to an increase of the PbSe bandgap from 0.15 (bulk bandgap) to 0.45 eV.

Li et al. [120] investigated the electrodeposition of PbSe films on indium tin oxide glass substrates. The solution contained 0.01 M $Pb(CH_3CO_2)_2$, 0.001 M SeO_2 and 0.1 M EDTA (pH 4). At the potential of −0.7 V vs. SCE, the reddish selenium films were deposited while silvery lead films were deposited at −0.9 V. Slightly Se-rich PbSe thin films were obtained at −0.8 V. The maximum film thickness of ∼400 nm was achieved by a 20 min deposition. After 20 min, the film thickness decreased slightly due to bad adhesion. The as-deposited PbSe films were polycrystalline and randomly oriented.

As mentioned above, the UPD potential range for PbTe overlaps with that for PbSe in an acidic nitrate bath, making the electrodeposition of $PbSe_{1-x}Te_x$ straightforward. Streltsov et al. [121] reported the electrodeposition of $PbSe_{1-x}Te_x$ films from acidic nitrate baths. They found that UPD of $PbSe_{1-x}Te_x$ could be achieved in the potential range of −0.1 to −0.4 V vs. Ag/AgCl (sat'd KCl). In this potential range, deposition potential had little influence on the film composition.

Sima et al. [122] electrodeposited $PbSe_{1-x}Te_x$ nanorods from a solution containing 0.05 M $Pb(NO_3)_2$, 0.001 M H_2SeO_3, 0.0006 M TeO_2, and 0.1 M HNO_3 at −0.337 V vs. SCE. Polycarbonate ion track membranes (Makrofol N, Bayer Leverkussen) of ∼30 μm thick were used as nanotemplates. When the pore diameter of the template was ∼100 nm, solid $PbSe_{1-x}Te_x$ nanorods were electrodeposited. While $PbSe_{1-x}Te_x$ microtubes were obtained when the pore diameter was ∼2000 nm. The growth of microtubes instead of nanorods was attributed to the higher deposition current when the pore diameter was bigger.

2.8. Electrodeposition of $CoSb_3$

$CoSb_3$ is a member of a large family of compounds which crystallize with the cubic skutterudite structure ($CoAs_3$), space group *Im*3 and eight AB_3 groups in the unit cell [123,124]. The optimum working temperature for thermoelectric based on $CoSb_3$ is around 600 K. The main challenge associated with the electrodeposition of

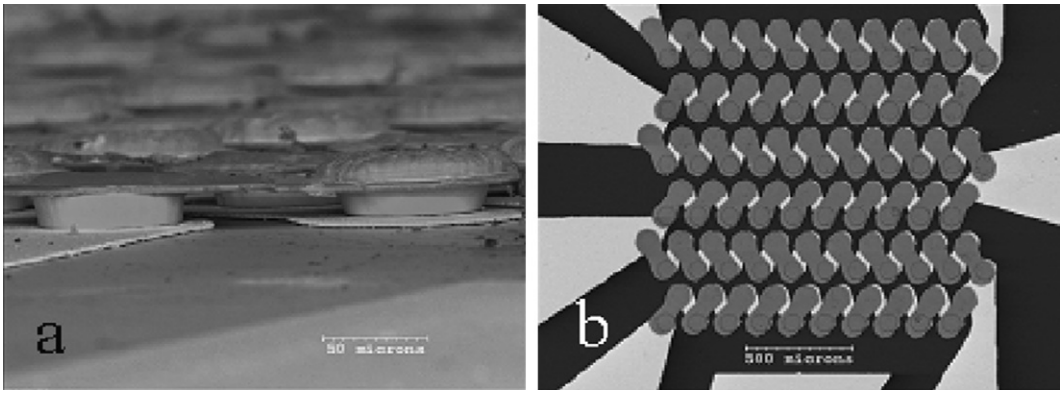

Fig. 12. (a) SEM image of a completed p-/n-type couple (∼20 μm height); (b) SEM overview of entire completed mircodevice. Reprinted with permission from ref. [128]. Copyright [2002] IEEE.

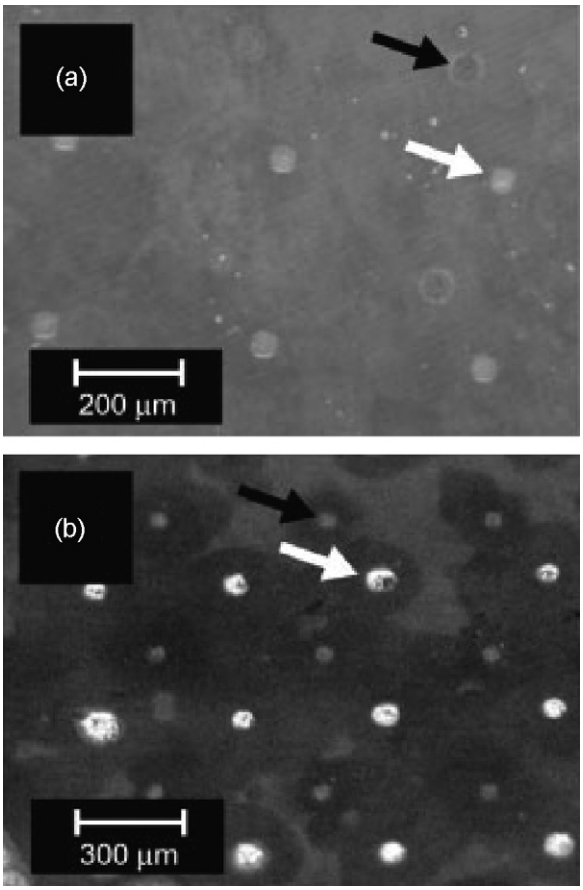

Fig. 13. Optical images of (a) underlying planarized gold-capped Bi_2Te_3 nanowire bundles (black arrow) with 50 μm diameter second holes patterned in the sacrificial photoresist, exposing the underlying parylene which is ready for O_2 RIE (white arrow); (b) array of 50 μm gold-capped Bi_2Te_3 nanowire bundles (black arrow) and unplanarized $Bi_{2-x}Sb_xTe_3$ nanowire bundles (white arrow) within the same nanotemplate. Reprinted with permission from ref. [129]. Copyright [2005] Wiley-VCH Verlag GmbH & Co. KGaA.

$CoSb_3$ from an aqueous solution is the disparate reduction potential of Co(II) and Sb(III). Under acidic conditions, the standard reduction potentials of the redox couples: Co^{2+}/Co^0 and SbO^+/Sb^0 are −0.28 and 0.212 V vs. SHE, respectively, which is 0.492 V apart [106]. Such a big separation makes it very difficult to achieve comparable deposition rates for Co and Sb and has produced only a couple of available reports on electrodeposited $CoSb_3$.

Behnke et al. [125] investigated the feasibility to electrodeposit $CoSb_3$ thin films and nanowires by pulse plating technique. The bath for thin film deposition consisted of 0.003 M Sb_2O_3, 0.688 M $CoSO_4$, 0.125 M potassium citrate, and 0.196 M citric acid. For nanowire depositions, the Co^{2+} concentration was reduced to 0.172 M. During the pulse plating, a layer of antimony was deposited at one potential, then at a more negative potential both cobalt and antimony were deposited. By oscillating between these two potentials and controlling the time at each potential, the average stoichiometry of the deposit was controlled. After pulse plating, the samples was annealed to react the antimony and cobalt to form $CoSb_3$. A sample was produced by pulsing for 0.3 s at −1.2 V (vs. Hg/Hg_2SO_4) followed by 0.1 s at −1.4 V. The complete deposition ran for 30 min. The sample was then annealed at 400 °C for 24 h. EDS analysis showed a Co/Sb ratio of ∼1/3. But the XRD pattern revealed the presence of Co phase in the deposit.

After 7 years, another work was reported on the electrodeposition of $CoSb_3$ by Chen et al. [126]. They fabricated 60 nm $CoSb_3$ nanowires by electrodeposition using home-made alumina membranes as nanotemplates. The electrolyte consisted of 0.01 M SbO^+, 0.10 M Co^{2+}, and 0.14 M tartaric acid. The pH of the solution was adjusted to 2.5 by adding 1 M HCl. The exact deposition potential was not declared. EDS analysis of as-deposited nanowires showed a stoichiometric composition; XRD pattern indicated that the nanowires were single $CoSb_3$ phase and preferentially oriented along with {4 2 0} planes.

3. Device fabrication

The ideal thermoelectric device contains hundreds of p–n junctions connected electrically in series to build up a higher voltage, but thermally in parallel between two planar surfaces to carry the heat, thus posing the challenge for nanostructured thermoelectric devices [127]. A miniaturized device will enable potentially thousands of p–n junctions to be connected together in a very small area, therefore increasing the maximum cooling and improving cooling densities. Snyder et al. [11,128] developed a novel and low cost electrochemical MEMS (microelectromechanical systems) process to fabricate three-dimensional thermoelectric microdevices. This process combined integrated circuit processing techniques and electrochemical deposition of n-type Bi_2Te_3 and p-type $Bi_{2-x}Sb_xTe_3$. A 400 μm thick oxidized silicon was used as a substrate to achieve a high thermal conductance. The bottom electrical interconnects of ∼3 μm Au were first fabricated by patterned electrodeposition and selective etching. Then a thick layer (20 μm) of positive photoresist was spin coated and a pattern of 60 μm holes in diameter was developed. After that, p-type $Bi_{2-x}Sb_xTe_3$ leg elements were electrodeposited at constant potential. After electrodeposition of the p-type material and deposition of a thin photoresist cover layer on top of the thick photoresist layer, the second hole pattern with a slight offset was developed for electrodeposition of n-type Bi_2Te_3 leg elements. After the growth of both p- and n-legs, a flood exposure (no mask) removed the cover photoresist layer and a very thin layer of gold was sputtered over the entire sample. Then the top nickel interconnects of 2–3 μm thick were fabricated through patterned electrodeposition and selective etching. The final device (Fig. 12) was annealed in forming gas (7.2% H_2 in Ar) at 250 °C for 2 h to improve the ZT of the thermoelectric materials as well as the mechanical and electrical contacts inside the device.

Lim et al. [129] demonstrated the fabrication of nanowire based thermoelectric device. Anodized alumina membrane was used as the nanotemplate. The nanotemplate was first sputtered on one side with a thin layer of gold, and then mounted onto a Au/Ti silicon substrate using silver paste. Next, an approximately 1 μm thick layer of parylene C was deposited over the entire nanotemplate. The parylene can form a continuous layer without penetrating into the nanotemplate pores. Then, a 3 μm thick layer of photoresist was spin-coated over the nanotemplate and patterned with an array of 50 μm holes. Using oxygen reactive-ion etching (RIE), the photoresist was used as a sacrificial layer while the exposed parylene was etched away. Next, n-type Bi_2Te_3 nanowire bundles were electrodeposited at the exposed areas. Then, the exposed areas were overfilled by electrodeposition of gold on top of the Bi_2Te_3 nanowires. After planarization, the patterning steps were repeated to create the second hole opening (Fig. 13a), followed by p-type $Bi_{2-x}Sb_xTe_3$ electrodeposition. After the fabrication of gold-capped Bi_2Te_3 and $Bi_{2-x}Sb_xTe_3$ bundled nanowire elements (Fig. 13b), the sample was ready for top and bottom interconnects.

4. Conclusion

Electrodeposition is a cost-effective and high through-put method to synthesize thermoelectric thin films and nanostructures, both of which will be crucial for commercialization. Numerous works have demonstrated that the material composition, crystallographic structure, and properties can be easily tuned by adjusting the electrochemical conditions such as deposition potential/current, electrolyte composition, substrate, etc. Through a template-directed electrodeposition process, thermoelectric nanowires of various materials can also be easily synthesized, a task that would otherwise prove to be difficult to impossible by other deposition techniques. However to date, most of the work on electrodeposited thermoelectric thin films and nanostructures focuses on synthesis, primarily investigating compositions and structure. A dissonant gap between synthesis and characterization of the thermoelectric properties, namely the Seebeck coefficient and thermoelectric figure of merit, creates only a partial picture for published works on electrodeposited thermoelectric materials. While composition and structure of electrodeposits are crucial indicators of physical properties, their measured thermoelectric performance will ultimately dictate their usefulness for various applications.

This lack of characterization is more true and perhaps most challenging for nanostructured thermoelectric materials, which face several hurdles. First and foremost, isolation of a known number of nanowires with known cross sectional areas is necessary to accurately measure the electrical resistivity and thermal conductivity of nanomaterials, which would be impossible with a nanowire array. In addition, four-point probe measurements are usually implemented to overcome contact resistance, requiring a lateral configuration also not compatible with nanoporous templates. However, the greatest disadvantage to nanoporous alumina templates is its large thermal conductivity. Consequently, to achieve thermal isolation nanowires must be suspended in air or in some cases contribution from other materials can be calculated out. Some systems also require heaters and temperature sensors to measure thermopower and thermal conductivity independently. Moreover, this intricate configuration must be fabricated small enough to effectively interface materials at the nanoscale level. Other complications that can occur are deteriorated ZT values from surface oxides that form from exposure to template etchants and air. Weak mechanical properties may also afflict single nanowire characterization attempts.

Device fabrication based on thermoelectric nanowires remains an arduous task due to the small sizes and complex arrangement, thermally in parallel and electrically in series, as indicated by the limited number of publications on the topic. While a couple of innovative reports have shown lithographic approaches to create devices with micropillars and nanowire bundles, little evidence is given in terms of device performance enhancement. This is probably due to the larger size of the micropillars and the high thermal conductivity of the alumina template in the case of the nanowire bundles. By and large, these results point to an integration or materials problem as opposed to a synthesis problem.

Since theoretical calculations first predicted drastic ZT improvements for thermoelectric nanowires, well beyond the stagnant bulk value of 1, significant progress has been made in synthesizing these structures via electrodeposition. Most of the electroplating baths were developed first for thin films and then demonstrated for nanowires using nanoporous templates. While electrodeposition continues unrivaled in terms of synthesis control current efforts in the field must address new issues to see its maturation. The most critical are the need for more quantitative analysis of thermoelectric properties and device fabrication strategies for thermoelectric nanowires. These endeavors have the potential to yield the ultimate goal for thermoelectric systems, efficient solid-state devices for cooling and harvesting waste thermal energy. Addressing these challenges will require an interdisciplinary approach, which may be fueled by attention from recent advances on thermoelectric nanostructures.

Acknowledgements

We acknowledge the financial support from Korea Institute of Materials Science (KIMS) and JPL/NASA Bio/Nano Program.

References

[1] W.S. Capinski, H.J. Maris, T. Ruf, M. Cardona, K. Ploog, D.S. Katzer, Physical Review B 59 (1999) 8105.
[2] M.S. Dresselhaus, Y.M. Lin, G. Dresselhaus, X. Sun, Z. Zhang, S.B. Cronin, T. Koga, J.Y. Ying, The Eighteenth International Conference on Thermoelectrics, Baltimore, MD, USA, 1999, p. 92.
[3] L.D. Hicks, M.S. Dresselhaus, Physical Review B 47 (1993) 16631.
[4] L.D. Hicks, T.C. Harman, X. Sun, M.S. Dresselhaus, Physical Review B 53 (1996) 10493.
[5] G.D. Mahan, H.B. Lyon, Journal of Applied Physics 76 (1994) 1899.
[6] R. Venkatasubramanian, E. Siivola, T. Colpitts, B. O'Quinn, Nature 413 (2001) 597.
[7] M.S. Dresselhaus, G. Dresselhaus, X. Sun, Z. Zhang, S.B. Cronin, T. Koga, J.Y. Ying, G. Chen, Microscale Thermophysical Engineering 3 (1999) 89.
[8] T.C. Harman, P.J. Taylor, D.L. Spears, M.P. Walsh, Journal of Electronic Materials 29 (2000) L1.
[9] D.Y. Li, Y. Wu, R. Fan, P.D. Yang, A. Majumdar, Applied Physics Letters 83 (2003) 3186.
[10] Y.D. Li, J.W. Wang, Z.X. Deng, Y.Y. Wu, X.M. Sun, D.P. Yu, P.D. Yang, Journal of the American Chemical Society 123 (2001) 9904.
[11] G.J. Snyder, J.R. Lim, C.K. Huang, J.P. Fleurial, Nature Materials 2 (2003) 528.
[12] S. Furuyama, T. Iida, S. Matsui, M. Akasaka, K. Nishio, Y. Takanashi, Journal of Alloys and Compounds 415 (2006) 251.
[13] D.L. Greenaway, G. Harbeke, Journal of Physics and Chemistry of Solids 26 (1965) 1585.
[14] B. Lenoir, A. Dauscher, M. Cassart, Y.I. Ravich, H. Scherrer, Journal of Physics and Chemistry of Solids 59 (1998) 129.
[15] H. Scherrer, S. Scherrer, in: R. David, Lide (Eds.), CRC Handbook of Chemistry and Physics, CRC Press, Boca Raton, FL, 1996, p. 211.
[16] J.O. Sofo, G.D. Mahan, Physical Review B 58 (1998) 15620.
[17] T.M. Tritt, Science 283 (1999) 804.
[18] F. Besse, C. Boulanger, B. Bolle, J.J. Heimann, Scripta Materialia 54 (2006) 1111.
[19] A. Boukai, K. Xu, J.R. Heath, Advanced Materials 18 (2006) 864.
[20] Y.M. Lin, X.Z. Sun, M.S. Dresselhaus, Physical Review B 62 (2000) 4610.
[21] X. Sun, Z. Zhang, M.S. Dresselhaus, Applied Physics Letters 74 (1999) 4005.
[22] G.D. Mahan, J.O. Sofo, Proceedings of the National Academy of Sciences of the United States of America 93 (1996) 7436.
[23] M.F. O'Dwyer, T.E. Humphrey, H. Linke, Nanotechnology 17 (2006) S338.
[24] C.L. Chien, F.Y. Yang, K. Liu, D.H. Reich, P.C. Searson, Journal of Applied Physics 87 (2000) 4659.
[25] P.M. Vereecken, L. Sun, P.C. Searson, M. Tanase, D.H. Reich, C.L. Chien, Journal of Applied Physics 88 (2000) 6529.
[26] F.Y. Yang, K. Liu, C.L. Chien, P.C. Searson, Physical Review Letters 82 (1999) 3328.
[27] F.Y. Yang, K. Liu, K.M. Hong, D.H. Reich, P.C. Searson, C.L. Chien, Science 284 (1999) 1335.
[28] P.M. Vereecken, K. Rodbell, C.X. Ji, P.C. Searson, Applied Physics Letters 86 (2005) 121916.
[29] S.B. Sadale, P.S. Patil, Solid State Ionics 167 (2004) 273.
[30] M.L. Yang, Z.B. Hu, Journal of Electroanalytical Chemistry 583 (2005) 46.
[31] K.M. Hong, F.Y. Yang, K. Liu, D.H. Reich, P.C. Searson, C.L. Chien, F.F. Balakirev, G.S. Boebinger, Journal of Applied Physics 85 (1999) 6184.
[32] K. Liu, C.L. Chien, P.C. Searson, Physical Review B 58 (1998) 14681.
[33] K. Liu, C.L. Chien, P.C. Searson, Y.Z. Kui, Applied Physics Letters 73 (1998) 1436.
[34] C.G. Jin, G.W. Jiang, W.F. Liu, W.L. Cai, L.Z. Yao, Z. Yao, X.G. Li, Journal of Materials Chemistry 13 (2003) 1743.
[35] L. Li, Y. Zhang, G.H. Li, W.H. Song, L.D. Zhang, Applied Physics a-Materials Science & Processing 80 (2005) 1053.
[36] L. Li, Y. Zhang, G.H. Li, X.W. Wang, L.D. Zhang, Materials Letters 59 (2005) 1223.
[37] L. Li, Y. Zhang, G.H. Li, L.D. Zhang, Chemical Physics Letters 378 (2003) 244.
[38] L. Li, Y. Zhang, Y.W. Yang, X.H. Huang, G.H. Li, L.D. Zhang, Applied Physics Letters 87 (2005) 031912.
[39] L. Li, Y.W. Yang, X.H. Huang, G.H. Li, R. Ang, L.D. Zhang, Applied Physics Letters 88 (2006) 103119.
[40] R. Martin-Lopez, A. Dauscher, H. Scherrer, J. Hejtmanek, H. Kenzari, B. Lenoir, Applied, Physics A-Materials Science & Processing 68 (1999) 597.
[41] G.E. Smith, R. Wolfe, Journal of Applied Physics 33 (1962) 841.

[42] W.M. Yim, A. Amith, Solid-State Electronics 15 (1972) 1141.
[43] Y.M. Lin, O. Rabin, S.B. Cronin, J.Y. Ying, M.S. Dresselhaus, Applied Physics Letters 81 (2002) 2403.
[44] F. Besse, C. Boulanger, J.M. Lecuire, Journal of Applied Electrochemistry 30 (2000) 385.
[45] P.M. Vereecken, S. Ren, L. Sun, P.C. Searson, Journal of the Electrochemical Society 150 (2003) C131.
[46] M. Martin-Gonzalez, A.L. Prieto, M.S. Knox, R. Gronsky, T. Sands, A.M. Stacy, Chemistry of Materials 15 (2003) 1676.
[47] A.L. Prieto, M. Martin-Gonzalez, J. Keyani, R. Gronsky, T. Sands, A.M. Stacy, Journal of the American Chemical Society 125 (2003) 2388.
[48] L. Li, G.H. Li, Y. Zhang, Y.W. Yang, L.D. Zhang, Journal of Physical Chemistry B 108 (2004) 19380.
[49] F.H. Xue, G.T. Fei, B. Wu, P. Cui, L.D. Zhang, Journal of the American Chemical Society 127 (2005) 15348.
[50] T.M. Tritt, M.A. Subramanian, MRS Bulletin 31 (2006) 188.
[51] F.D. Rosi, B. Abeles, R.V. Jensen, Journal of Physics and Chemistry of Solids 10 (1959) 191.
[52] M. Takahashi, Y. Katou, K. Nagata, S. Furuta, Thin Solid Films 240 (1994) 70.
[53] M. Takahashi, Y. Oda, T. Ogino, S. Furuta, Journal of the Electrochemical Society 140 (1993) 2550.
[54] M. Takahashi, Y. Muramatsu, T. Suzuki, S. Sato, M. Watanabe, K. Wakita, T. Uchida, Journal of the Electrochemical Society 150 (2003) C169.
[55] P. Magri, C. Boulanger, J.M. Lecuire, Journal of Materials Chemistry 6 (1996) 773.
[56] S. Michel, S. Diliberto, C. Boulanger, N. Stein, J.M. Lecuire, Journal of Crystal Growth 277 (2005) 274.
[57] S. Michel, S. Diliberto, C. Boulanger, B. Bolle, Journal of Crystal Growth 296 (2006) 227.
[58] M. Martin-Gonzalez, A.L. Prieto, R. Gronsky, T. Sands, A.M. Stacy, Journal of the Electrochemical Society 149 (2002) C546.
[59] K. Tittes, A. Bund, W. Plieth, A. Bentien, S. Paschen, M. Plotner, H. Grafe, W.J. Fischer, Journal of Solid State Electrochemistry 7 (2003) 714.
[60] W. Zhu, J.Y. Yang, X.H. Gao, S.Q. Bao, X.A. Fan, T.J. Zhang, K. Cui, Electrochimica Acta 50 (2005).
[61] B.W. Gregory, J.L. Stickney, Journal of Electroanalytical Chemistry 300 (1991) 543.
[62] B.H. Flowers, T.L. Wade, J.W. Garvey, M. Lay, U. Happek, J.L. Stickney, Journal of Electroanalytical Chemistry 524 (2002) 273.
[63] F. Forni, M. Innocenti, G. Pezzatini, M.L. Foresti, Electrochimica Acta 45 (2000) 3225.
[64] D.W. Suggs, I. Villegas, B.W. Gregory, J.L. Stickney, Journal of Vacuum Science & Technology A—Vacuum Surfaces and Films 10 (1992) 886.
[65] W. Zhu, J.Y. Yang, J. Hou, X.H. Gao, S.Q. Bao, X.A. Fan, Journal of Electroanalytical Chemistry 585 (2005) 83.
[66] Y. Miyazaki, T. Kajitani, Journal of Crystal Growth 229 (2001) 542.
[67] Y.H. Lee, K.Y. Lee, J.S. Bae, J.H. Lee, J.Y. Byun, D.B. Hyun, T.S. Oh, Designing, Processing and Properties of Advanced Engineering Materials 449-4 (Pts 1 and 2) (2004) 377.
[68] B.Y. Yoo, C.K. Huang, J.R. Lim, J. Herman, M.A. Ryan, J.P. Fleurial, N.V. Myung, Electrochimica Acta 50 (2005) 4371.
[69] S.H. Li, M.S. Toprak, H.M.A. Soliman, J. Zhou, M. Muhammed, D. Platzek, E. Muller, Chemistry of Materials 18 (2006) 3627.
[70] P. Heo, K. Hagiwara, R. Ichino, M. Okido, Journal of the Electrochemical Society 153 (2006) C213.
[71] S.A. Sapp, B.B. Lakshmi, C.R. Martin, Advanced Materials 11 (1999) 402.
[72] A.L. Prieto, M.S. Sander, M. Martin-Gonzalez, R. Gronsky, T. Sands, A.M. Stacy, Journal of the American Chemical Society 123 (2001) 7160.
[73] M.S. Sander, R. Gronsky, T. Sands, A.M. Stacy, Chemistry of Materials 15 (2003) 335.
[74] M.S. Sander, A.L. Prieto, R. Gronsky, T. Sands, A.M. Stacy, Advanced Materials 14 (2002) 665.
[75] C.G. Jin, X.Q. Xiang, C. Jia, W.F. Liu, W.L. Cai, L.Z. Yao, X.G. Li, Journal of Physical Chemistry B 108 (2004) 1844.
[76] W.L. Wang, C.C. Wan, Y.Y. Wang, Journal of Physical Chemistry B 110 (2006) 12974.
[77] L. Li, Y.W. Yang, X.H. Huang, G.H. Li, L.D. Zhang, Nanotechnology 17 (2006) 1706.
[78] X.C. Xu, L.D. Chen, C.F. Wang, Q. Yao, C.D. Feng, Journal of Solid State Chemistry 178 (2005) 2163.
[79] W. Wang, Q.H. Huang, F.L. Jia, J. Zhu, Journal of Applied Physics 96 (2004) 615.
[80] J.H. Zhou, C.G. Jin, J.H. Seol, X.G. Li, L. Shi, Applied Physics Letters 87 (2005) 133109.
[81] E.J. Menke, M.A. Brown, Q. Li, J.C. Hemminger, R.M. Penner, Langmuir 22 (2006) 10564.
[82] E.J. Menke, Q. Li, R.M. Penner, Nano Letters 4 (2004) 2009.
[83] G. Leimkuhler, I. Kerkamm, R. Reineke-Koch, Journal of the Electrochemical Society 149 (2002) C474.
[84] C.F. Wang, Q. Wang, L.D. Chen, X.C. Xu, Q. Yao, Electrochemical and Solid State Letters 9 (2006) C147.
[85] J.Y. Yang, W. Zhu, X.H. Gao, S.Q. Bao, M. Fan, X.K. Duan, J. Hou, Journal of Physical Chemistry B 110 (2006) 4599.
[86] D. Del Frari, S. Diliberto, N. Stein, C. Boulanger, J.M. Lecuire, Thin Solid Films 483 (2005) 44.
[87] D. Del Frari, S. Diliberto, N. Stein, C. Boulanger, J.M. Lecuire, Journal of Applied Electrochemistry 36 (2006) 449.
[88] M. Martin-Gonzalez, A.L. Prieto, R. Gronsky, T. Sands, A.M. Stacy, Advanced Materials 15 (2003) 1003.
[89] C.G. Jin, G.Q. Zhang, T. Qian, X.G. Li, Z. Yao, Journal of Physical Chemistry B 109 (2005) 1430.
[90] F. Xiao, B.Y. Yoo, K.H. Lee, N.S.V. Myung, Nanotechnology 18 (2007) 335203.
[91] B. Yoo, F. Xiao, K.N. Bozhilov, J. Herman, M.A. Ryan, N.V. Myung, Advanced Materials 19 (2007) 296.
[92] A.P. Torane, C.D. Lokhande, P.S. Patil, C.H. Bhosale, Materials Chemistry and Physics 55 (1998) 51.
[93] J.D. Desai, Bulletin of Electrochemistry 15 (1999) 315.
[94] S. Michel, N. Stein, M. Schneider, C. Boulanger, J.M. Lecuire, Journal of Applied Electrochemistry 33 (2003) 23.
[95] M. Martin-Gonzalez, G.J. Snyder, A.L. Prieto, R. Gronsky, T. Sands, A.M. Stacy, Nano Letters 3 (2003) 973.
[96] L.X. Bu, W. Wang, H. Wang, Applied Surface Science 253 (2007) 3360.
[97] C. Wood, Reports on Progress in Physics 51 (1988) 459.
[98] David Michael Rowe, CRC Handbook of Thermoelectrics, CRC Press, Boca Raton, FL, 1995, p. 701.
[99] Z.H. Dughaish, Physica B-Condensed Matter 322 (2002) 205.
[100] H. Saloniemi, T. Kanniainen, M. Ritala, M. Leskela, Thin Solid Films 326 (1998) 78.
[101] H. Saloniemi, M. Kemell, P. Ritala, M. Leskela, Journal of Electroanalytical Chemistry 482 (2000) 139.
[102] L. Beaunier, H. Cachet, R. Cortes, M. Froment, Journal of Electroanalytical Chemistry 532 (2002) 215.
[103] Y.A. Ivanova, D.K. Ivanou, E.A. Streltsov, Electrochemistry Communications 9 (2007) 599.
[104] F. Xiao, B. Yoo, M.A. Ryan, K.H. Lee, N.V. Myung, Electrochimica Acta 52 (2006) 1101.
[105] F. Xiao, B. Yoo, K.N. Bozhilov, K.H. Lee, N.V. Myung, Journal of Physical Chemistry C 111 (2007) 11397.
[106] R. David, Lide, CRC Handbook of Chemistry and Physics, 87th ed., CRC Press, Cleveland, OH, 2006.
[107] A.N. Molin, A.I. Dikusar, Thin Solid Films 265 (1995) 3.
[108] H. Saloniemi, T. Kanniainen, M. Ritala, M. Leskela, R. Lappalainen, Journal of Materials Chemistry 8 (1998) 651.
[109] H. Saloniemi, M. Kemell, M. Ritala, M. Leskela, Journal of Materials Chemistry 10 (2000) 519.
[110] E.A. Streltsov, N.P. Osipovich, L.S. Ivashkevich, A.S. Lyakhov, V.V. Sviridov, Electrochimica Acta 43 (1998) 869.
[111] E.A. Streltsov, N.P. Osipovich, L.S. Ivashkevich, A.S. Lyakhov, Electrochimica Acta 44 (1999) 2645.
[112] D.K. Ivanou, E.A. Streltsov, A.K. Fedotov, A.V. Mazanik, Thin Solid Films 487 (2005) 49.
[113] D.K. Ivanou, E.A. Streltsov, A.K. Fedotov, A.V. Mazanik, D. Fink, A. Petrov, Thin Solid Films 490 (2005) 154.
[114] L. Beaunier, H. Cachet, R. Cortes, M. Froment, Electrochemistry Communications 2 (2000) 508.
[115] L. Beaunier, H. Cachet, M. Froment, Materials Science in Semiconductor Processing 4 (2001) 433.
[116] M. Froment, L. Beaunier, H. Cachet, A. Etcheberry, Journal of the Electrochemical Society 150 (2003) C89.
[117] R. Vaidyanathan, S.M. Cox, U. Happek, D. Banga, M.K. Mathe, J.L. Stickney, Langmuir 22 (2006) 10590.
[118] R. Vaidyanathan, J.L. Stickney, U. Happek, Electrochimica Acta 49 (2004) 1321.
[119] Z. Hens, E.S. Kooij, G. Allan, B. Grandidier, D. Vanmaekelbergh, Nanotechnology 16 (2005) 339.
[120] K.W. Li, X.T. Meng, X. Liang, H. Wang, H. Yan, Journal of Solid State Electrochemistry 10 (2006) 48.
[121] E.A. Streltsov, N.P. Osipovich, L.S. Ivashkevich, A.S. Lyakhov, Electrochimica Acta 44 (1998) 407.
[122] M. Sima, I. Enculescu, T. Visan, R. Spohr, C. Trautmann, Molecular Crystals and Liquid Crystals 418 (2004) 749.
[123] T. Caillat, J.P. Fleurial, A. Borshchevsky, Journal of Crystal Growth 166 (1996) 722.
[124] D.T. Morelli, T. Caillat, J.P. Fleurial, A. Borshchevsky, J. Vandersande, B. Chen, C. Uher, Physical Review B 51 (1995) 9622.
[125] J.F. Behnke, A.L. Prieto, A.M. Stacy, T. Sands, The Eighteenth International Conference on Thermoelectrics, Baltimore, MD, USA, 1999, p. 451.
[126] L.J. Chen, H.N. Hu, Y.X. Li, G.F. Chen, S.Y. Yu, G.H. Wu, Chemistry Letters 35 (2006) 170.
[127] F.J. DiSalvo, Science 285 (1999) 703.
[128] J.R. Lim, G.J. Snyder, C.-K. Huang, J.A. Herman, M.A. Ryan, J.-P. Fleurial, The Twenty-First International Conference on Thermoelectrics, 2002, p. 535.
[129] J.R. Lim, J.F. Whitacre, J.P. Fleurial, C.K. Huang, M.A. Ryan, N.V. Myung, Advanced Materials 17 (2005) 1488.